TOPOLOGICAL ORIGIN OF THE URBACH TAIL

A dissertation presented to

the faculty of

the College of Arts and Sciences of Ohio University

In partial fulfillment

of the requirements for the degree

Doctor of Philosophy

Yue Pan

March 2009

This dissertation entitled

TOPOLOGICAL ORIGIN OF THE URBACH TAIL

by

YUE PAN

has been approved for

the Department of Physics and Astronomy

and the College of Arts and Sciences of Ohio University by

_____

David A. Drabold

Distinguished Professor of Physics

_____

Benjamin M. Ogles

Dean, College of Arts and Sciences

PAN, YUE, Ph.D., March 2009, Physics and Astronomy

Topological Origin of the Urbach Tail (102pp.)

Director of Dissertation: David A. Drabold

Urbach tail, the universal exponential band tail observed in impure crystals and disordered materials, was first identified in 1953. Despite theories presented to explain the Urbach tail, the topological origin of this nearly universal phenomenon still remains unknown. The topological nature of the band tail states with the Urbach tail energies is important for the understanding of several properties of amorphous material including, for instance, electronic transport. The main target of my study is to determine the topological origin of the Urbach tail and develop a basic understanding of the problem. My study is carried out via the investigation of networks of high quality amorphous silicon for topological details and via *ab intio* calculations for electronic properties. In this dissertation, the *topological filaments*, and the *electronic filaments*, reflecting topology-electron correlation, are defined and observed. The band tail states are directly related to explicit topological elements (correlations) and the topological origin of Urbach tail is identified in at least one important material. Alongside the study of the Urbach tail, a semi-quantitative scattering theory is presented to explain basic electronic quantities of amorphous solid. Electron transport in solids and Boron doping a-Si:H are also studied: results are concisely presented.

Approved: _____

David A. Drabold

Distinguished Professor of Physics

Acknowledgments

I need to thank my colleagues Dr. Mingliang Zhang and F. Inam. Your collaboration and your help during the course of my study were essential to the completion of my dissertation. I need to thank my advisor, Dr. Drabold, for offering this great opportunity to me for completing my doctoral degree and your guiding help throughout my study. I need to thank the Department of Physics and Astronomy of Ohio University for the opportunity and the help.

I need to mention my thankfulness for my wife, Beina, who has always been there for me. I also would like to thank my father and my mother, for your support through these years, morally and financially.

And also, all the advisors and teachers that have ever helped me, thank you. All the family members and best friends at home, thank you.

Table of Contents

List of Tables

List of Figures

CHAPTER 1

Introduction

Urbach tail[1], the exponential band tail observed in impure crystals and disordered materials, was first identified by F. Urbach in 1953. Although theories have been presented to explain the Urbach tail, no correlation to the topology of the network has ever been made. The origin of this universal phenomenon still remains unknown. The nature of three-dimensional space-filling disordered networks is salient to a variety of topics in scientific research. The exact topology of the band tail states directly related to the Urbach tail, for instance, is important for modeling electronic transport in amorphous materials, since the electronic hopping takes place between these localized states.

The main target of my study presented in this dissertation is to determine the topological origin of the Urbach tail and develop a basic understanding of the problem. My study is carried out via the investigation of high quality amorphous silicon models for topological details and via *ab intio* calculations for electronic properties. Alongside the study of the Urbach tail, a semi-quantitative scattering theory is presented to explain basic electronic quantities of amorphous solid. I also study electron transport in solids. Kubo-Greenwood[2, 3] formula is implemented into *ab inito* code for calculating AC and DC conductivity of solids. Furthermore, Boron doping of a-Si:H is studied, addressing the low doping efficiency problem.

1.1 Amorphous solid

1.1.1 Structure of amorphous materials

The atomic ordering is usually categorized into three length scales: short range order (SRO), medium range order (MRO) and long range order (LRO). The key difference between amorphous solid (AS) crystalline solid (CS) is the absence of long range order[4]. The short range chemical order in amorphous solid (AS), is usually similar to their crystalline counterpart. A clear difference between amorphous solid (AS) and crystalline solid (CS) can usually be seen in *radial distribution functions* (RDF) (closely related to the *pair correlation function*). The first peak (first neighbor distance) of the RDF of amorphous solid is usually well defined while further peaks are increasingly smoothed out, indicating an absence of LRO.

1.1.2 Defects

A defect is a consequence of extreme topological and/or chemical disorder present in an amorphous solid. In an elemental solid, defect can be categorized into two types: *coordination defect* and *strain defect*. Term *coordination defect* is used for those atoms that have a coordination number (number of neighbors) different than "8-N" rule[5]. In a-Si, it includes three bonded site: the dangling bond, and five bonded site: the "floating" bond. Electronically, coordination defects create mid-optical-gap states and these states are highly localized in space. Term *strain defect* designates badly strained sites. In a-Si, these sites usually maintain fourfold

bonding but the bond angles and bond lengths (strongly) deviate from the crystalline structure. Topological distortions from ideal bonding are commonly recognized as the origin of the band tail states: the main object of our study for this dissertation.

1.1.3 Electronic density of states (EDOS)

The electronic density of states (EDOS) of amorphous solid (AS) is visibly altered from that of the crystalline solid (CS) with broadened peaks (smoothed van Hove singularities) and most importantly the band tails decaying into the optical gap where the EDOS for CS vanishes. It was a surprise that scientists discovered the existence of the optical gap in AS with a gap comparable to crystal. The persistence of the optical gap has been roughly understood as the result of the existence of short range order (SRO) in AS[6].

1.1.4 Localized state

The localized state is one of most important concepts of solid state physics. P. W. Anderson advanced this concept 50 years ago[8]. Depending on the electronic structure of the materials, there exist insulator-metal transition (the Mott transition, only in highly correlated systems) and disorder-induced localization (the Anderson transition). Our focus involves material a-Si and a-Si:H, where typical Anderson transition takes place. All localization phenomena in this dissertation are therefore disorder-induced localizations. For further background of this topic, please refer to [4].

With recent development of the *ab initio* calculation, electronic structure of amorphous solid can now be obtained by first principles. The picture of localized states have been much better visualized. J. Dong and D. A. Drabold demonstrated the qualitative nature of the Anderson transition via study of a 4096 Si model[10]. For very localized states, which arise from defects, most of the electron charge is localized in a spatially compact *single-island* region. Moving into the band, the localization level (IPR) decreases and electronic *multi-islands* start to appear in space and form the "quasiextended" states. Further into the band, states are completely extended. J. Dong and D. A. Drabold introduced the important *resonant cluster proliferation* concept to qualitatively explain how the transition took place and the energy dependence of the localized states. Later J. J. Ludlam et al[11] showed the universality of the picture via a 10,000-atom Si model and varied interactions and disorder.

1.1.5   The Urbach tail

The character of the tail states in disordered semiconductors is a problem of importance with a history dating back to the fifties. It has been understood that band tail states in amorphous semiconductors arise from strains in the network sufficient to push states past the band edges into the gap. Such tails decay exponentially (not as a Gaussian) into the gap: this feature, nearly universal to disordered semiconductors, is called Urbach tailing[1], which was first identified by F. Urbach at the edges of op-

tical interband and excitonic transitions in impure crystals[1]. Clever photoemission experiments allow the separate observation of the valence and conduction tails and even the temperature dependence of the tailing[12].

Exponential band edges have since been observed in a wide variety of materials, mostly via optical absorption. This feature is surprisingly universal as it has been observed in every amorphous solids and imperfect crystalline solids. The universality of the Urbach tail suggests the possibility of a common underlying cause. Theoretical attempts to explain the phenomenon were however limited, with the most recent attempt by M. H. Cohen and coworkers [13, 14] nearly twenty years ago. At the time, those theories could not connect the electronic structure to any specific topological units. For this dissertation, my main goal is to, via powerful first principle calculation tools, examine the internal structure of models of amorphous Si and locate the structural origin of the Urbach tails. By connecting underlying topology to the electronic structure of the Urbach tail, I look forward to a basic understanding of this universal phenomenon.

1.1.6 Electron transport

Carrier transport in a-Si can be described via hopping through localized states. The transitions are induced by phonon vibrations. For this type of transport mechanism, the best estimation of the conductivity is via the Kubo-Greenwood formula[2, 3] (Eq. 1.1).

$$\sigma(\omega) = \frac{2\pi e^2 \hbar}{Vm^2} \sum_{ni} \left| \left\langle \psi_n \left| \hat{P} \right| \psi_i \right\rangle \right|^2 \frac{f_F(\varepsilon_i) - f_F(\varepsilon_n)}{\hbar\omega} \delta(\varepsilon_n - \varepsilon_i - \omega) \qquad (1.1)$$

where f_F is the Fermi function (distribution), e and m are the electronic charge and mass, V is the cell volume, $\hat{P}$ the momentum operator, ψ_i and ϵ_i are the eigenstates and eigenvalues. A detailed description is presented in Appendix A. In his paper[27], T. A. Abtew et al for the first time implemented Kubo-Greenwood formula into *ab intio* code SIESTA. Our current effort presented in this dissertation can be regarded a continuation of T. A. Abtew's work. We again implement a thermally averaged Kubo-Greenwood formula into the newly introduced code SIESTA 2.0[15] and added the AC conductivity calculation utility in addition to the DC conductivity calculation. Since much of the basic theory has been presented elsewhere, this work has been relegated to appendices, which will nevertheless be useful to future researchers in this field.

1.2 Modeling

For *ab initio* or empirical computational study of amorphous materials, experimentally realistic models are essential. Modeling methods have been introduced and improved over the past twenty years. For Si, usual modeling methods include: Molecular Dynamics method, Activation relaxation technique, Monte Carlo techniques, Reverse Monte Carlo techniques and WWW algorithm[28]. All these methods are involved in the models we study.

The Molecular Dynamics (MD) method is used to generate amorphous structure through a melt-quenching simulation. MD method only requires a valid potential energy function, and in principle might yield the dynamic processed that occur in the real material. There are clear drawbacks of this method. The output structure from this method always contains a large fraction of coordination defects which are not present in a real amorphous material. Therefore the radial distribution function (also called pair correlation function) has a shoulder before the second peak indicating high strains in the structure. EDOS is also incorrect with many defect-induced gap states.

Activation relaxation technique ART[29] is a method designed to avoid being stuck in a local energy minimum of the energy landscape. ART does not attempt to reproduce the dynamics of the atoms. Instead, it seeks events involving crossing over an energy barrier. This approach directly yields rare diffusive events. ART is designed for systems with many local minima. The drawback of the method, however, is that ART is computationally expensive and difficult to use with an *ab initio* interaction potential.

The Reverse Monte Carlo (RMC) method is a technique for generating structural configuration based on experimental data (constraints). RMC starts with a randomly generated system. For every set of experimental data, there is a constraint (cost) function. RMC then randomly displaces a (or a group) of atom(s) and estimates the cost functions. The probability that new state will be accepted depends

on the satisfaction of the cost functions. RMC is a fast method and is still under development.

The WWW algorithm[28] was designed by Wooten, Weaire and Winer for the purpose of generating high quality amorphous structure (CRN). In the WWW approach, a CRN consists of the positions of N atoms and an explicit list of the 2N bonds between them. The structural evolution of the network is produced by a sequence of Monte Carlo moves called bond transpositions. The generation of a CRN starts with a crystalline or randomized system. The network is then relaxed through a sequence of bond transpositions. The WWW algorithm has been proven to be the "gold standard" for making realistic models. A decade later B. R. Djordjevic, M. F. Thorpe and F. Wooten[32] used the same approach with more computing power to generate a set of a-Si models including two 4096-atom models. These models exhibit even better quality in terms of low defects and low strains.

In this dissertation, the majority of the models studied are WWW/DTW models. One ART model and two RMC models are used. In addition, a-Si:H and B doped a-Si:H models include MD process, based on WWW/DTW starting structures. In terms of defects these models are comparable and all in high quality (small bond-angle distributions). Structural quantities and EDOS are all close to experiment data.

1.3   Methods employed

Density functional theory (DFT) and associated methods are the most widely used approximate first principle approach in computational materials science. Density functional theory[7] (DFT) is built on the assertion (proved by Hohenberg, Kohn and Mermin) that the electron density of any system determines all ground-state properties of the system, that is, $E=E[n_0]$, where n_0 is the ground-state electron density of the system. Many-body electronic wavefunction can thus be replaced with the electronic density as the basic variable to describe the ground state. Whereas the many-body wavefunction is dependent on 3N variables with complex symmetry properties, the density is only a function of three variables and is a simpler quantity to deal with both conceptually and practically. The calculation of electronic structure in many-body systems like solids and molecules has been made practical since the introduction of density functional theory.

The issues associated with density functional theory are that first, the exact form of the universal energy density functional is unknown. Second, extension to excited states is not obvious. It is the Kohn-Sham ansatz that made possible the approach to replace the original many-body problem by a practical single particle problem. This can lead to independent-particle equations of non-interacting system with the most difficult many-body terms from the original Hamiltonian incorporated into an exchange-correlation functional E_{xc} of the density. The ground state density

and energy of the original interacting system can be found with the accuracy limited only by the approximations in the exchange-correlation functional.

Authoritative treatments of DFT and full details of its implementation are available in R. Martin's book[7].

1.4 SIESTA 2.0 package[15]

SIESTA 2.0[15] is an improved *ab initio* calculation package over successful SIESTA. SIESTA 2.0 is the main tool for all the first principle calculations presented in this dissertation. SIESTA 2.0 is DFT[7] based: the exchange-correlation potential is inserted by LDA or GGA approximation and can be chosen by user. SIESTA 2.0 applies full selfconsistency for solving the Kohn-Sham equation. Harris functional is available for faster and cruder calculation. SIESTA 2.0 applies linear combination of atomic orbital (LCAO) basis set. As a contrast, plane wave basis set is an alternative approach. LCAO basis set means fewer basis functions and faster computation compared to the plane wave basis set especially for localized wavefunctions. SIESTA 2.0 uses standard non-local, norm-conserving psedopotentials for the estimation of inter-atomic interactions. SIESTA 2.0 offers a variety of simulations including molecular dynamics, relaxations, vibrational properties (phonons) and more. SIESTA 2.0 generates the Kohn-Sham eigenvalues, wavefunction, forces, stress, atomic position and velocities for the given system. For the materials we study, i.e. a-Si, a-Si:H,

boron doped a-Si:H and Al etc., SIESTA 2.0's results have been consistently reliable and comparable to available experiment data.

1.5 Outline of the dissertation

Our Urbach tail study begins from Chapter 2 as we attempt to understand the problem by the simplest model. We try to connect band tail energy with individual distortion units such as bond-angle or bond-length. The simple model, however, is tested and confirmed to be flawed: local individual distortion units directly connected to the Urbach tail can not be found. However, hints of certain form of topology-electron correlation is revealed during the process. We continue the Urbach study in Chapter 3. We firstly discover the topological correlation (the topological filaments) underlying the random networks. We then reveal general features in the structure of the band tail electron states, especially the existence of 1D filamentary structure associated with chains of long and short bonds. Both bond-length distortions and bond-angle distortions have been found to be correlated to the band tail states, in a collective fashion: rather than individual distorted units, the 1D filaments (both electronic and topological) are viewed as the units that are connected to the eigenstates. We then point out the direct relation between the topological filaments and the formation of the Urbach exponential decay; we argue that the topological filaments are the root of the Urbach tailing. We then provide computational evidences to support the hypothesis. In Chapter 4, we attempt to explain several basic, yet

important quantities of a-Si by semi-quantitative scattering approaches. Study of the low efficiency of B doping is presented in Chapter 5. The conductivity calculations are included in Appendix A.

The content and results presented in chapter 3 have been published in two papers: Y. Pan, M. Zhang and D. A. Drabold, J. Non. Cryst. Sol. **354** 3480 (2008) [18]; and Y. Pan, F. Inam, M. Zhang and D. A. Drabold, Phys. Rev. Lett. **100** 206403 (2008) [19]. While the majority of the content written in this dissertation is extracted from my own work, F. Inam is an important collaborator in the study. His main contribution includes creation of point-like defects in c-Si and the removal of topological correlations. These supply key evidences for establishing relation between topological filaments and the Urbach tails. Meanwhile, M. Zhang provided important theoretical supports for organizing concepts and explaining quantities. The content and results presented in Chapter 4 are submitted: Mingliang Zhang, Yue Pan, F. Inam and D. A. Drabold, Phys. Rev. Lett. (5/2008). [54]. The main content of the chapter is extracted from M. Zhang's work. My study of the Urbach tails and corresponding findings provides the basis for the theory to be created upon. Also I supply calculation of the IPRs and the extraction of the Urbach energies which are presented in the chapter.

CHAPTER 2

A preliminary study of the origin

of the Urbach tail in amorphous Si

2.1 Overview

"There is an extensive literature calculating the position of the mobility edge with various simple models, but it has not yet proved possible to do this for a "continuous random network" such as that postulated for SiO_2, As_2Se_3, amorphous Si or any amorphous material where the coordination number remains the same as in the crystal. This problem is going to be quite a challenge for the theoreticians - but up till now we depend on experiments for the answer, particularly those in which electrons are injected into a non-crystalline material..." [From Mott's Nobel Lecture[16], 1977]

The nature of three-dimensional space-filling disordered networks is salient to a variety of topics in scientific research. Despite work in recent decades, a number of puzzles remain both about the structure and connectivity of such networks. Also, important quantities *derived from* such structures (such as electronic or vibrational states) are quite incompletely understood, though their characteristics are ultimately derived from the underlying structure.

With the development of computational modeling, realistic computations of the materials has become possible. Dong and Drabold[34] have attempted to correlate the local distortions to Urbach tailing in an earlier study, based on the fact that the topological (i.e. bond-angle and bond-length) distortions are found to be normally distributed. An isomorphic one-to-one correspondence between a local distortion and the energy of a localized state was assumed. We now temporarily call this conjecture by the short name *the "one-to-one" picture*. In this picture, each single topological distortion (a bond-angle or a bond-length) is the root of a certain localized state, and the sum of all these states naturally leads to a Urbach exponential decay, involving that fact that the local distortion is Gaussian distributed.

At the time a detailed inspection of the topology was not available and the conjecture stayed more at a hypothetical than a confirmed stage. To further investigate the theory, we now examine our a-Si networks in more detail. We currently have an array of realistic a-Si models available from 64 to 100,000 atoms in size. These models provides a wealth of topological information. Meanwhile and most importantly, we are now able to calculate the Mulliken charge of the eigenstates and the "one-to-one" conjecture can be tested.

2.2 A simple conjecture

It is a property of realistic WWW models that Gaussian distribution of bond-length and cosine of bond-angle is exhibited in a-Si (see Fig. 3.1). Using $\zeta = \cos\theta$,

normal distribution is in the form,

$$P(\zeta) = \frac{1}{\sigma\sqrt{2\pi}}e^{-\frac{(\zeta-\zeta_0)^2}{2\sigma^2}} \tag{2.1}$$

where ζ_0 is the average cosine of the bond-angle. In a-Si, $\zeta_0 \approx \cos(109.5^o)$; σ is the broadening factor. The one-to-one conjecture can be described in short form. If we have (1) Gaussian distribution as in eq (2.1), and (2) energy associated with the distortion has parabolic form $\varepsilon = A(\zeta - \zeta_0)^2 + \varepsilon_o$, then we have an Urbach tail (exponential decay of density of states) in the form of $f(\varepsilon) \propto e^{-(\varepsilon-\varepsilon_o)/c}$. Here ε_o can be regarded as the *mobility edge*. For a valence tail, we assume $\varepsilon - \varepsilon_o \geq 0$; for a conduction tail, we assume $\varepsilon - \varepsilon_o \leq 0$.

The one-to-one conjecture is mathematically simple. Let us use $\epsilon = (\varepsilon - \varepsilon_o)$ and $\xi = (\zeta - \zeta_0)$, then we have $A\xi^2 = \epsilon$, or $\xi = \pm\sqrt{\frac{\epsilon}{A}}$. Also

$$2A\xi d\xi = d\epsilon \tag{2.2}$$

We can write the distribution in term of ϵ.

$$P(\xi)d\xi = f(\epsilon)\left|\frac{d\epsilon}{d\xi}\right|d\xi \tag{2.3}$$

$$[\frac{1}{\sigma\sqrt{2\pi}}e^{-\frac{\xi^2}{2\sigma^2}}]d\xi = f(\epsilon)\left|2A\xi\right|d\xi \tag{2.4}$$

$$\frac{1}{\sigma\sqrt{2\pi}}e^{-\frac{\epsilon}{2A\sigma^2}} = f(\epsilon)2\sqrt{A\epsilon} \tag{2.5}$$

$$f(\epsilon) = \frac{1}{2\sqrt{A\epsilon}} \frac{1}{\sigma\sqrt{2\pi}} e^{-\frac{\epsilon}{2A\sigma^2}} \tag{2.6}$$

Or

$$f(\varepsilon) = \frac{1}{\sigma\sqrt{8\pi A}} \frac{1}{\sqrt{(\varepsilon - \varepsilon_o)}} e^{-\frac{(\varepsilon - \varepsilon_o)}{2A\sigma^2}} \tag{2.7}$$

There is a subdominant term $\frac{1}{\sqrt{(\varepsilon - \varepsilon_o)}}$ in the prefactor. However, the strong exponential decay term should dominate the behavior and this is still considered an exponential form of energy ε.

2.3   The Distortions

Now we already have the Gaussian distributions as a starting point, we then only need to prove that the relation between local distortion and its correspondent energy is $\varepsilon = A(\zeta - \zeta_0)^2 + \varepsilon_o$. As you can see the ideal network to show our picture should be defect-free model. "Defect" here means the coordination defect: three-coordinated "dangling bond" or five-coordinated "floating bond" would introduce in-gap state, and in our understanding, generally does not contribute to the exponential form of the tails. Worse, in-gap states might contaminate the exponential tailing and induce other effects. For these reasons, coordination defects are avoided.

We use a 512 DTW (as discussed in Chapter 1) defect-free a-Si model and a 4096 DTW defect-rare (0.3%) a-Si model. We look for the local distortion in the following way. For each very localized state, i.e, a state deep in the exponential tail,

we pick the atom that contains the most charge. Then we start looking for geometrical distortion around that particular atom. We soon run into trouble. The fact is that there are four bonds and six bond-angles starting from an atom. So what is the local distortion associated with that site? We also realized that the localized charge, for each state, does not always involve a highly distorted unit. i.e. a badly distorted bond-length or bond-angle, even for some highly localized states. Thus there must be something more subtle at work.

A rule still has to be set for linking the corresponding individual distortion to the state. And we reach a compromise: starting from the atom which contains the most charge, we pick the neighboring atom that contains the most charge among the four neighbors. This provides us with a single bond, which involves the largest amount of charge, for a localized state. We plot this bond-length in Figure 2.1 and Figure 2.2 against the energy for model DTW512 and DTW4096. Similarly, we pick the two neighboring atoms that have the most charge among the four neighbors, and this provides us with a bond-angle with arguably the most charge from the localized state. We also plot this bond-angle in Figure 2.1 and Figure 2.2. For model DTW4096, only a small portion of data near the Fermi level (0.0eV) is shown.
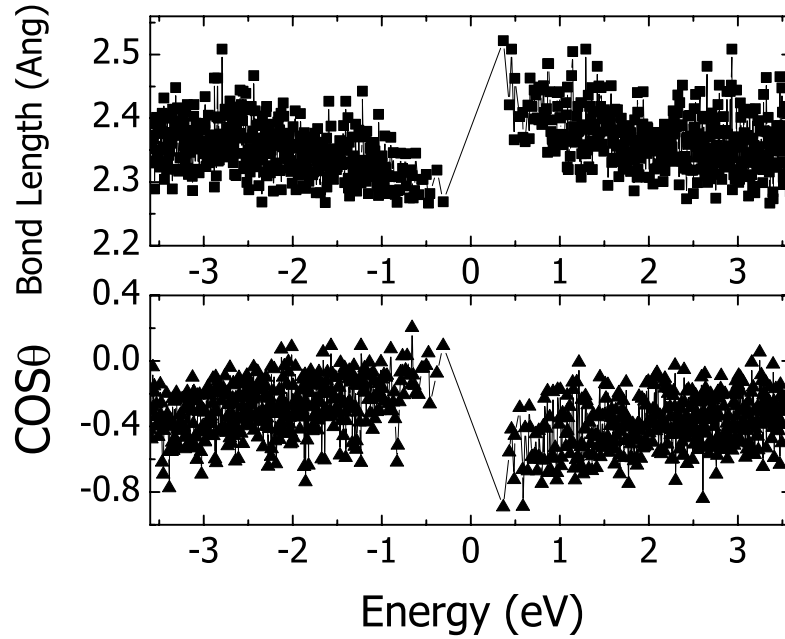
Figure 2.1: Model DTW512. Single distorted bond-length and bond-angle, plotted against eigen-energy. Fermi level lies at 0.0 eV. Refer to the text for detailed description.

2.4 Results

2.4.1 The negatives

Our one-to-one conjecture assumes every individual distortion (bond-length or bond-angle distortion) is the unique, underlying cause of a localized state. The summation of these distortions forms the Urbach tail. As we see in Figure 2.1 and Figure 2.2, firstly the signal is very noisy. Secondly they do not seem to be parabolic against energy, at least from the noisy appearance. One possible explanation for these issues is that we haven't found the "correct" single distortions for each state. To test
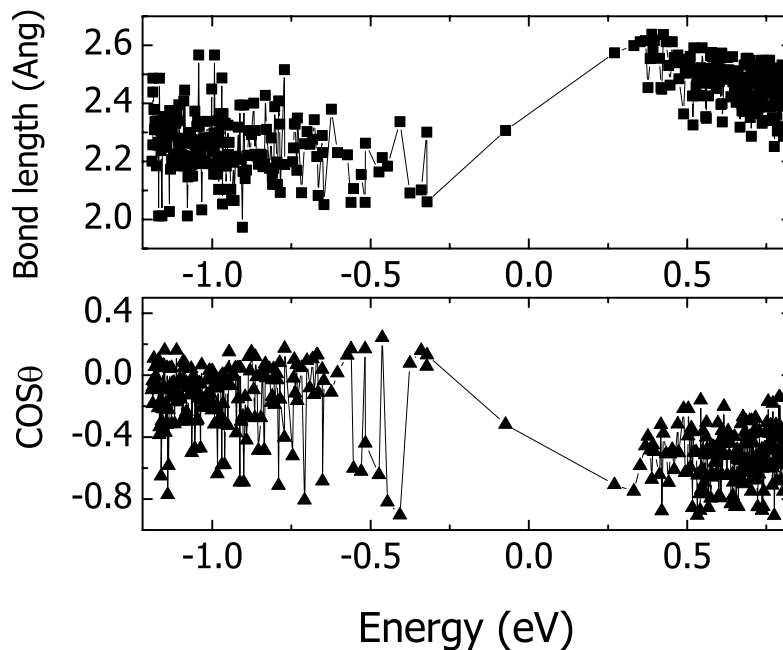
Figure 2.2: Model DTW4096. Single distorted bond-length and bond-angle plotted against eigen-energy. Fermi level lies at 0.0 eV. Only a small portion of data near the Fermi level is shown. Refer to the text for detailed description.

that, we have used several other algorithms to obtain the local distortions. None of them works significantly better, so far as "single-distortion" is concerned.

The reason, in our opinion, is that: "single distortion" or the "one-to-one" picture is too simple. The fact is that we observe that most localized states involve charge spreading over more than one distortion unit. It is true that in the extremely localized states, charge can be limited to only one or several atoms. But even in this case the distortions, as we observe among various cases, can be unclear: there can be no single highly-distorted bond or angle sitting near these charge centers. In addition,

the "extremely localized" region is only a tiny fraction of the spectrum (only about 1 state in our DTW512 model, and 7 states in DTW4096 model). Urbach tail spreads a range larger than the region. In many moderately localized states on the Urbach tail, the charge spreads over a number of atoms. It is natural in these atoms, there is no single distortion that stands out as the "representative" of the eigenstate. Therefore to reach the root of Urbach tail problem, groups of distortions rather than "single distortions" have to come into the picture. A collective behavior of the distortions needs to be explored for understand the Urbach tailing.

2.4.2   The positives

What we do learn from this simple one-to-one picture is nevertheless rewarding. (1)This is our first detailed observation of the topological distortions in the a-Si networks. (2)It confirms our basic assumption: the distortion is indeed connected to the eigen-energy. Stronger distortion, in general, is more likely to be found in the localized states than a non-localized states. (3)Although noisy, there is a visible and interesting trend for the distortions: the valence tail is more correlated with short bond-length and small bond-angle distortions; the conduction tail is more correlated with long bond-length and large bond-angle. (4)There is a hint of filament-like paths for the electronic charge.

Fedders, Drabold, Nakhmanson's study [25] observed that valence tail states preferentially involved short bond lengths, whereas conduction tail states tended to

be involved with longer bond lengths. Our noisy plots are consistent with the observations. We greatly enhance the study based on the observation (3) and (4) during the proceeding chapters.

2.5 Summary

We start our study for Urbach tail from assuming every individual geometrical distortion unit creates a band tail state. With the tool SIESTA and other computational methods, we obtain the Kohn-Sham eigenvalue and eigenvectors. Inspection of the local topology is made and we try to connect the eigenvectors to the local distortions. We report the approach to be flawed for Urbach tailing analysis as far as "one-to-one" conjecture is concerned. The information extracted from the attempt, however, still provides us hints of the nature of the problem and leads our study to the next chapter.

CHAPTER 3

Topological filament, electronic filament and the Urbach tail

*The content and results presented in this chapter are published: Y. Pan, M. Zhang and D. A. Drabold, J. Non. Cryst. Sol. **354** 3480 (2008) [18]; and Y. Pan, F. Inam, M. Zhang and D. A. Drabold, Phys. Rev. Lett. **100** 206403 (2008) [19].*

3.1 Introduction

Earlier exploration into Model DTW512 and Model DTW4096 (presented in Chapter 2) for topological distortions leaves us hints of possible interesting correlation to the electronic states. In this chapter, we extended our study to nine of our models, among which seven of them are closely inspected. We obtain the electronic states and calculate the eigenvectors and Mulliken charge populations for each eigenstate. Our main target is finding the topological origin associated with the band tail states and furthermore the Urbach tail.

The main body of this chapter consists of three sections. In section 3.2, consideration of several models reveals certain persistent geometrical features, notably strong self-correlations between configurations involving short bonds and analogous

correlations involving long bonds. We dub this feature the *topological filament (TF)*. These correlations exist in various structural models and survive *ab initio* thermal molecular dynamics (MD) simulations.

In section 3.3 we relate electronic charge of the band tail states in a-Si with general topological features. Fedders, Drabold, Nakhmanson's study [25] observed that valence tail states preferentially involved short bond lengths, whereas conduction tail states tended to be involved with longer bond lengths. Angle distortion was also mentioned but no specific relation to the band tails was detected. In addition, related work was undertaken in Ref. [26]. Here, we extend this analysis to our collection of models. In agreement with these earlier reports [25, 26], we confirm a robust tendency for valence (conduction) tail states to be associated with short (long) bonds. On the other hand, we for the first time detect analogous features for the bond angle distribution, where we see that smaller (larger) bond angles are correlated with valence (conduction) tails. In addition, we confirm the existence of *electronic filaments* (EF) for highly localized states, the hints of which were encountered earlier (mentioned in Chapter 2).

In section 3.4, the overlap between the topological filament and the electronic filament is investigated. We are not providing a full explanation for the exact mechanism of the overlap. Instead, we bring up a qualitative conjecture that the topological correlation (topological filaments) stand at the heart of the Urbach tails.

#	Author	NOA	Type	$\Delta\theta/\Delta\cos\theta$	Δb	De%
M_1	DTW [32]	512	WWW	$20.1°/0.33$	0.08	0.0
M_2	DTW [32]	4096	WWW	$19.1°/0.31$	0.19	0.2
M_3	Feldman [33]	1000	WWW	$18.4°/0.30$	0.08	4.0
M_4	Mousseau [29]	4000	ART[29]	$17.8°/0.30$	0.11	4.0
M_5	Nakhmanson [30]	1000	PC	N/A	N/A	0.0
M_6	Biswas [31]	216	RMC[31]	$22.3°/0.37$	0.30	12.5
M_7	Biswas [31]	500	RMC[31]	$22.5°/0.37$	0.24	12
M_8	Mousseau	64	WWW	$20.7°/0.34$	0.11	0.0
M_9	DTW [32]	216	WWW	$24.5°/0.40$	0.30	0.0

Table 3.1: Models and basic information. NOA stands for "Number of atoms"; De% stands for "defects percentage"; $\Delta\theta/\Delta\cos\theta$ stands for the width of bond-angle $\theta/\cos\theta$ distribution; Δb stands for the width of bond-length distribution; WWW stands for Wooten-Weaire-Winer modeling scheme [28]; ART stands for activation-relaxation technique [29]; PC stands for "paracrystalline"; RMC stands for Reverse Monte-Carlo modeling scheme [31].

3.2   Topological correlation - the topological filament

3.2.1   Model characteristics and nomenclature

Even in good quality unhydrogenated material, mid-gap defects are fairly rare, at most a few sites per thousand [5]. At a practical level this means that ideal models of tractable size (up to several thousand atoms) can contain zero to a few defects producing mid-gap states. The Wooten-Weaire-Winer (WWW) [28] method is the "gold standard" for forming such realistic models, and several of the models we discuss depend upon WWW at least as a starting point. For completeness, and in particular to ascertain the extent to which our observations might tend to be WWW artifacts, we have repeated the calculations for other models as well. We summarize some salient features of the models in Table 3.1.

M_1, M_2, M_3, M_8 and M_9 all derived originally from WWW[28] modeling scheme. M_1, M_2 and M_9 were developed by B. R. Djordjevic, M. F. Thorpe, F. Wooten [32]; M_3 was developed by Feldman and M_8 by N. Mousseau. M_4 was made via activation-relaxation technique [29]. M_5 and M_6 are Reverse-Monte-Carlo [31] models. Model M_1 to M_4 and M_6 to M_9 are continuous random network (CRN) models. Beside CRN models, we include model M_5, a paracrystalline model (CRN with crystalline inclusion). In particular for M_5, 211 crystalline silicon atoms are embedded.

Excepting M_5, all the models that we have studied here have normally distributed bond lengths and cosines of bond angles. For the large WWW models the similarity to the normal distribution is quite striking[34]. Here we report the bond length and bond angle distributions for these models in Fig. 3.1. Model M_1 and M_4 show nearly perfect Gaussian fits, while model M_7, (a 500-atom model), is fairly Gaussian, with statistical noise. The other models exhibit similar traits. Dong and Drabold[34] have attempted to correlate these normally-distributed quantities to Urbach tailing.

Model M_1, M_5, M_8 and M_9 are defect free. In the other models, there are coordination defects, ranging from 0.2% to 12.5%, including both dangling bonds and five-fold "floating" bonds. The pair correlation functions of these models are all similar, accurately reflecting the experimental function. As usual with a-Si, this is a
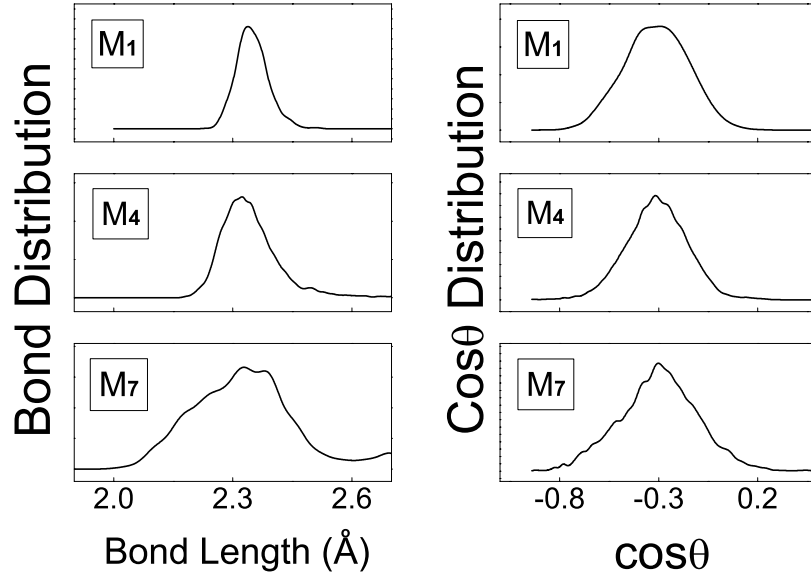
Figure 3.1: Bond length distributions and bond angle (cosθ) distributions.

reminder that the information in the pair-correlation function alone is very insufficient to specify coordinates.

3.2.2   Local inter-bond correlations

Our inspection of the topology of the models reveals that there is a tendency for short bonds to be linked to other short bonds and long bonds to be linked to other long bonds. In particular, this leads to 1) a tendency to spatial separation of the shortest and the longest bonds in the system; 2) a tendency to build up filament and ring like structures among extreme bonds. Selected fractions of shortest and longest bonds of model M_1 are extracted from the models and displayed in Fig. 3.2. The

correlation is clearly visible, especially in Fig. 3.2c-f. Interpenetrating filamentary structures appear to percolate through space for a sufficiently large cutoff in the fractions of bonds displayed. For comparison, the 4% shortest and 4% longest bonds of model M_2 - M_7 are shown in Fig. 3.3. To some extent, the self-correlations of short and long bonds are visible in every model shown, suggesting that such bond correlations are not an artifact of a particular model or modeling scheme.
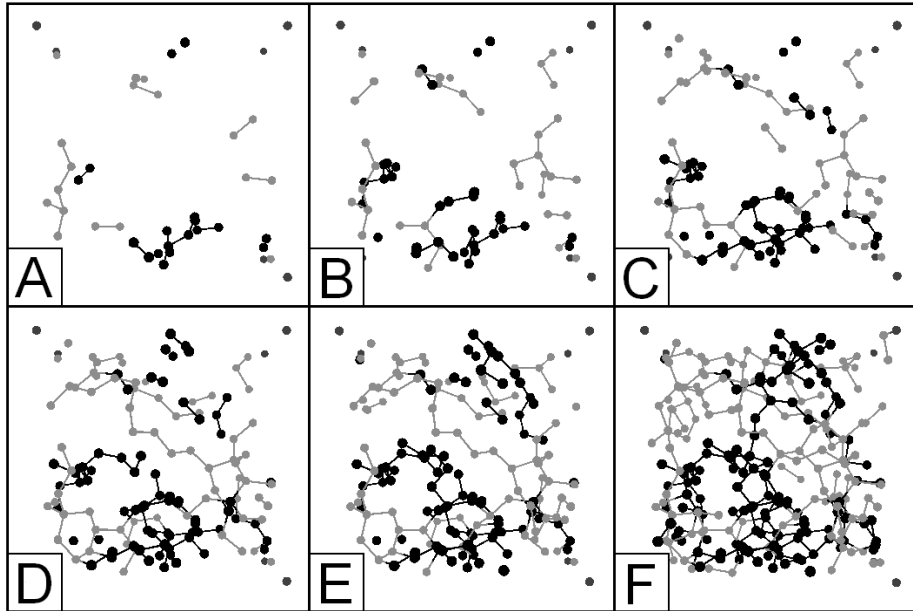
Figure 3.2: Shortest bond (dark) and longest bonds (light) in model DTW512 (M_1).

To explore our observation more quantitatively, we computed bond-bond correlation functions for the shortest and longest bonds:

$$\beta(r) = \frac{V}{4\pi r^2 N_1 N_2} \sum_{n_1=1}^{N_1} \sum_{n_2 \neq n_1}^{N_2} \delta(r_{n_1 n_2} - r) \qquad (3.1)$$
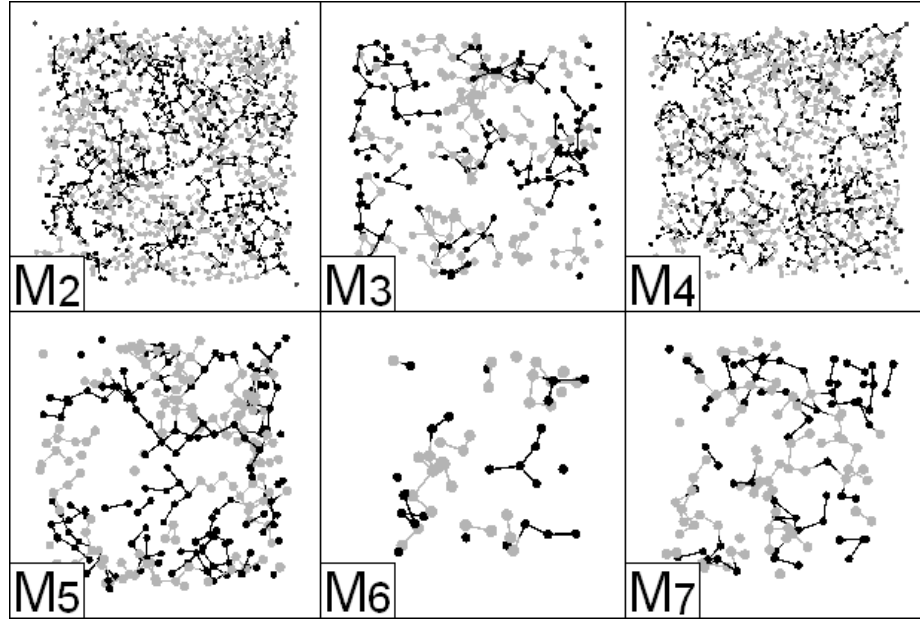
Figure 3.3: 4% shortest (dark) bonds and longest (light) bonds of 6 models.

where N_1, N_2 are the number of short or long bonds as needed; n_1 and n_2 count over these particular bonds; $r_{n_1 n_2}$ is the distance between the bond centers of bond n_1 and bond n_2; V is the volume of the unit cell. The 4% shortest and 4% longest bonds are taken for model M_1 and the corresponding bond-bond correlation functions for (1) $N_1 = 4\%$ shortest, $N_2 = 4\%$ longest; (2)$N_1 = 4\%$ shortest, $N_2 = 4\%$ shortest; (3) $N_1 = 4\%$ longest, $N_2 = 4\%$ longest are plotted in Fig. 3.4. The first peaks of the correlations of the same-type bonds (grey and dotted lines) appear to be much stronger than the correlation between the different-type bonds (solid black line). The second and even the third peaks maintain this feature, and after 6.0 Å, this correlation wanes. This confirms that there is a correlation among the same-type-bonds, with a correlation radius around $6.0 \mathring{A}$ for model M_1. The very similar correlation functions

between the 4% shortest and the 4% longest bonds of model M_2 - M_7 are plotted in Fig.3.5. A substantial correlation between same-type bonds is revealed for all models, with minor variations from model to model. Model M_1, M_3, M_5 and M_6 show slightly stronger effects than the rest. Model M_3 and M_5 show stronger correlations between the short bonds compared to those between the long bonds, while model M_6 and M_7 have relatively stronger correlations between the long bonds than those between the short bonds.
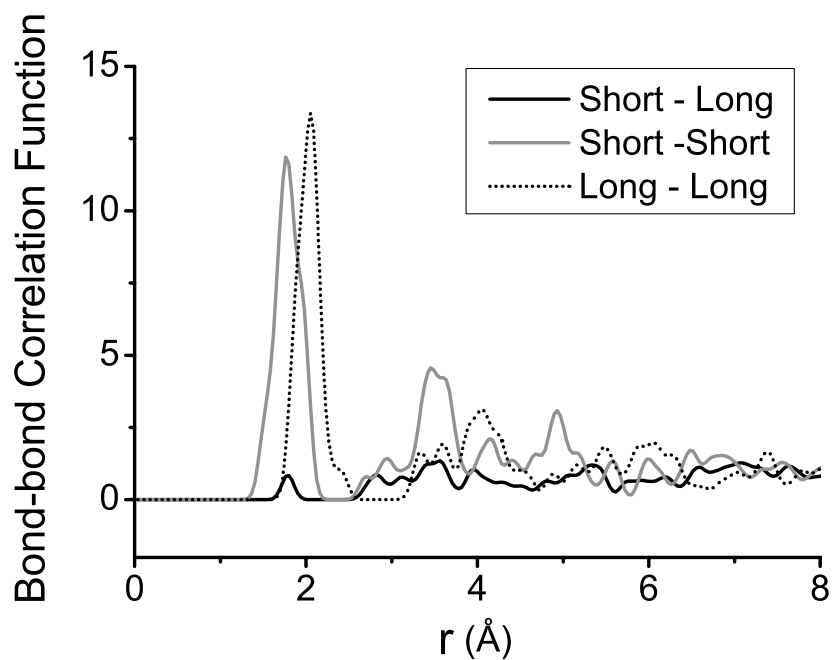
Figure 3.4: Pair correlation between bond centers of model DTW512 (M_1).
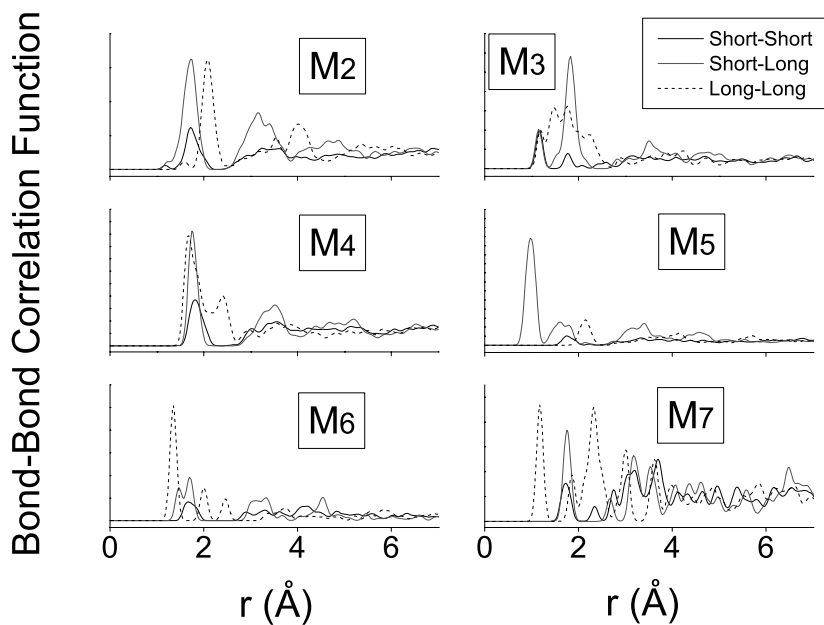
Figure 3.5: Pair correlations between bond centers for 6 models.

3.2.3 Persistence of correlation effects with *ab initio* relaxation

The correlations are found quite consistently in the several models we examined, suggesting that the effects are not modeling artifacts. We also undertook a simple comparison to see how a conjugate gradient (CG) relaxation process by SIESTA affects the models. A relaxation was done on model M_1 and M_9. While there were slight modifications in structure due to the CG process, we didn't observed any significant changes in these correlations.

3.2.4 Persistence of correlation at finite temperature

To further explore the likelihood that the long and short inter bond correlations were artifacts, we also undertook thermal MD simulations at 300K on two small models (M_8 and M_9) with the code SIESTA. Nosé dynamics were used. With some thermally-induced fluctuations, the short-short bond correlation and long-long bond correlation persist at all times, as seen in Fig. 3.6 for model M_9, where the heights of the first peaks of the pair correlation functions from Eq (3.1) are plotted throughout time steps. 4% shortest bonds and 4% longest bonds of the system at all time were involved for the calculations. The correlations between the same types of bonds are fluctuating but generally higher than that between the different types. The detailed temperature dependence in this correlation, however, requires further study.

3.2.5 Section summary

We have discovered a significant and reasonably model-independent feature of a-Si network namely the topological correlation. This correlation leads to short bond centers, long bond centers and filamentary linking paths in between. We call this topological correlation *the topological filament* (TF).
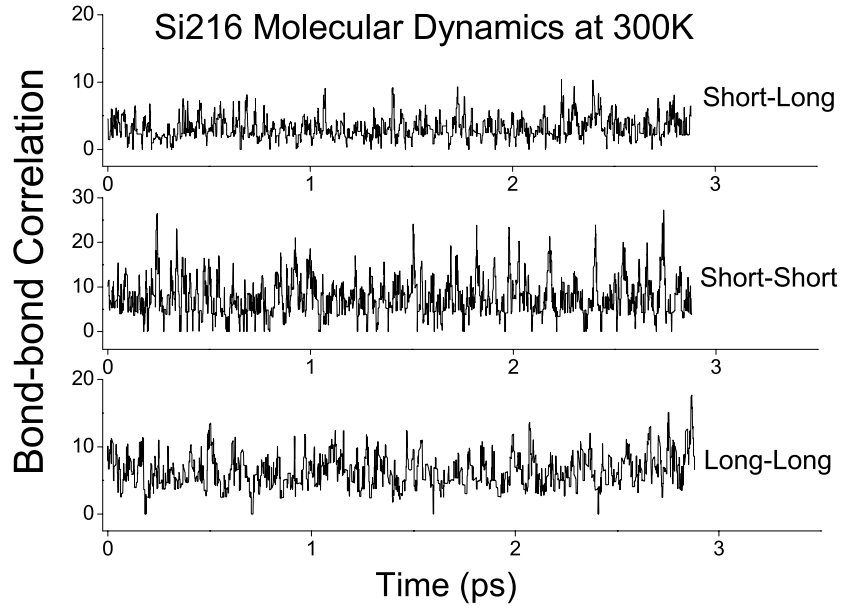
Figure 3.6: Bond-bond correlation under molecular dynamics. Model DTW216 (M_9) is used for 3000 fs.

3.3 Electron-topology correlation - the electronic filament

3.3.1 Density of states and Localization

The electronic and optical properties of the models are determined by the coordinates of the atoms. Electronic eigenstates and wavefunctions of the models are obtained for static lattices. For the larger model M_2 and M_4 a tight binding model [35, 36] is applied. For other models, the *ab initio* code SIESTA [15] is used. Results are very similar for the empirical and *ab initio* calculations.

Densities of states near E_f of the seven models are given in Fig.3.7. Spatial localization is reported using the Inverse Participation Ratio (IPR) in Fig. 3.8. Model
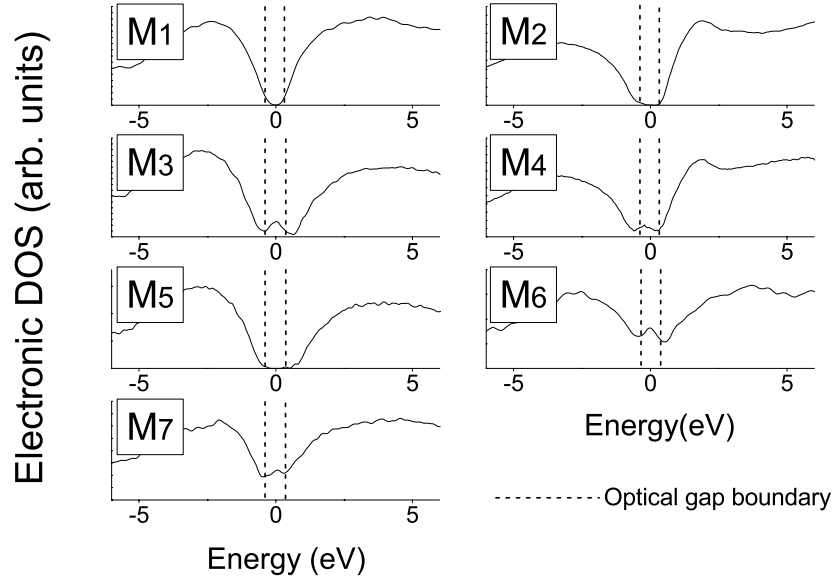
Figure 3.7: Density of states of the 7 models.

M_1 and M_5 are defect free, with no states in their optical gaps. Model M_2 has 0.2% defects and one gap state. Model M_3 and M_4 both have 4% defects, and a small peak of states in the gap. M_6 has 12.5% defects and M_7 has 12% defects and both have many states spread through the gap. Only M_1, M_2 and M_5 conform closely to ordinary expectations for an a-Si DOS. M_3, M_4, M_6 and M_7 exhibit too many defects for good a-Si materials and are studied here mainly for comparison purpose.

3.3.2 Bond length-electron correlations and bond angle-electron correlations near E_f

Fedders, Drabold, Nakhmanson's study [25] observed that valence tail states preferentially involved short bond lengths, whereas conduction tail states tended to
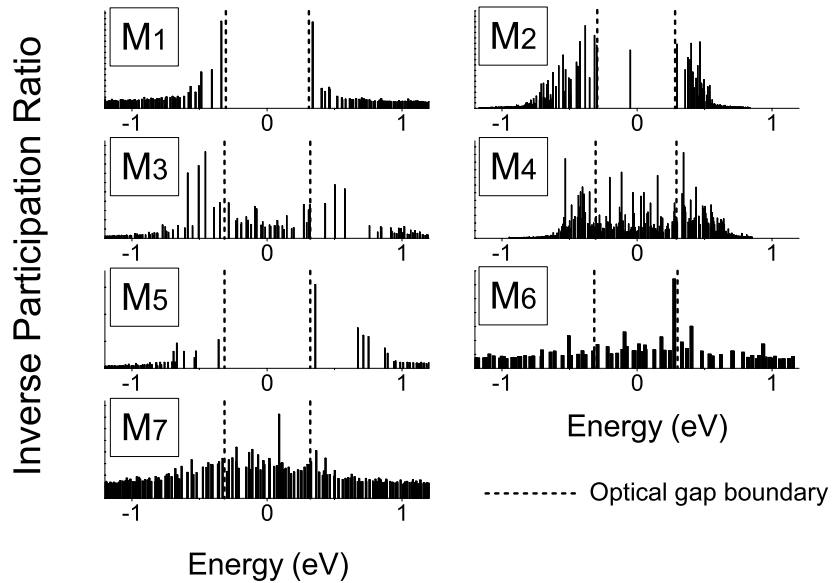
Figure 3.8: Inverse Participation Ratio of the 7 Models.

be involved with longer bond lengths. Angle distortion was also mentioned but no specific relation to the band tails was detected. Related work was undertaken in Ref. [26]. Here, we extend this analysis to our collection of models. Where the bond lengths are concerned, the present work is consistent with these findings. In addition we also clearly detect a correlation between valence tail and small bond angle, and a correlation between conduction tail and large bond angle, which has not been explicitly observed before.

An electron(Mulliken charge)-weighted mean bond length for each state was calculated in Ref. [25], and it revealed an interesting and general trend in bond lengths. Here we computed the mean bond length in a similar fashion, and explored

into seven of our models for this mean value. We then extended the calculations into the mean bond angles, using the very same Mulliken charge.

For a certain eigenstate E, the Mulliken charge $q_{(n,E)}$ is the electron probability on an atom n. Using it as a weighting factor, we define the corresponding symmetrized mean bond length as $B_{(E)}$.

$$B_{(E)} = \frac{\sum_{n,m} b_{(n,m)} q_{(n,E)} q_{(m,E)}}{\sum_{n,m} q_{(n,E)} q_{(m,E)}} \tag{3.2}$$

where n, m summations *only* go over all the possible bonds in a unit cell (of N atoms), with n, m as the bond end atoms. $q_{(n,E)}$, as defined, is the electron probability on the atom n. $B_{(E)}$ (near the Fermi level) for each model is plotted in Fig. 3.9. $B_{(E)}$ shows an asymmetrical split around the gap (Fermi level) for all models. Smaller average bond lengths are correlated to the valence tails and large average bond lengths correlated to the conduction tails. There are clear difference among the seven models, especially on the mid-gap states from the models with high defect concentration. For models with fewer defect states in the gap, the bond-electron correlations are very clear. Models with many mid-gap states show mixed behavior, though the asymmetric splitting is always detectable.

In analogy with the discussion for bond lengths, we define the electron-weighted mean of bond angles as:

$$A_{(E)} = \frac{\sum_{n,m,l} \theta_{(n,m,l)} q_{(n,E)} q_{(m,E)} q_{(l,E)}}{\sum_{n,m,l} q_{(n,E)} q_{(m,E)} q_{(l,E)}} \tag{3.3}$$

49
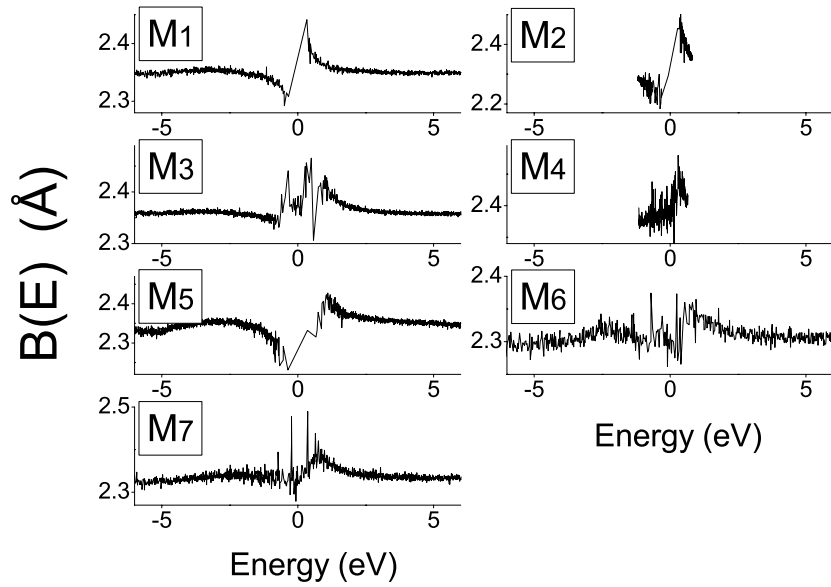
Figure 3.9: Charge-weighted averaged bond length of the 7 models.

where n, m, l are the atoms of the unit cell of N atoms; summations of n, m, l *only* count over all the possible bond angles, with m as the vertex of each angle. $q_{(n,E)}$, as defined, is the electron probability on the atom n. $A_{(E)}$ is plotted in Fig. 3.10. It also shows a clear asymmetrical splitting around the gap for all plots. Smaller average bond angles clearly appear to be correlated to the valence tails and larger average bond angles correlated to the conduction tails. There are also differences among the models but the asymmetric feature remains. Interestingly, these angle-electron correlations show strong resemblance to the bond-electron correlations discussed above.
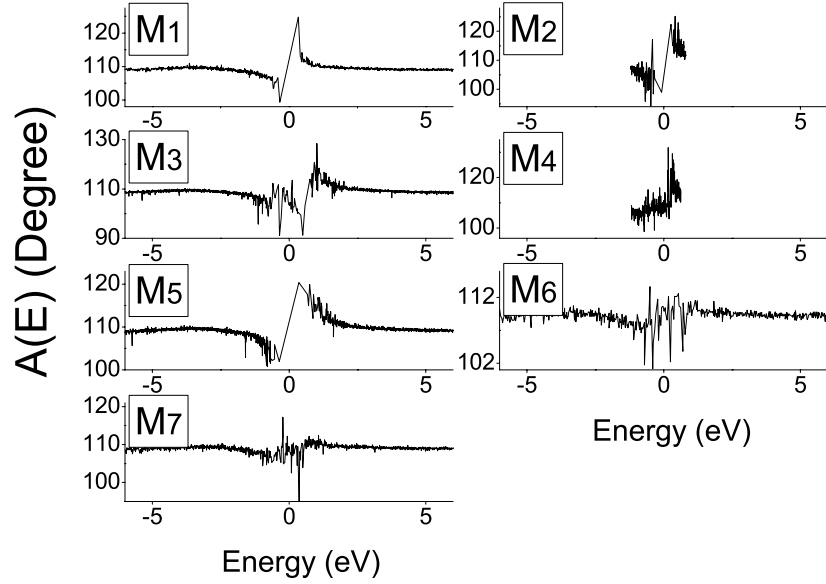
Figure 3.10: Charge-weighted averaged bond angle of the 7 models.

One feature to note is that here only the energies near the Fermi level are shown. In our models, $A_{(E)}$ and $B_{(E)}$ also have extrema in other spectral gaps, whenever the states are fairly localized.

3.3.3 Filamentary structure

During our initial inspections into the localized states, we found that the electron charge tended to spread over certain paths. The initial impression emerged that they were 1-D filament-like. We have now confirmed that the highly-localized states of model M_1 displays a 1-D filamentary connectivity. We extract 9 eigenstates for the band-tail states, 4 valence states and 5 conduction states, and display them

in the Figure 3.11. Interestingly, these localized states all happen to form 1-D-like filamentary charge paths, with occasional ring formations.
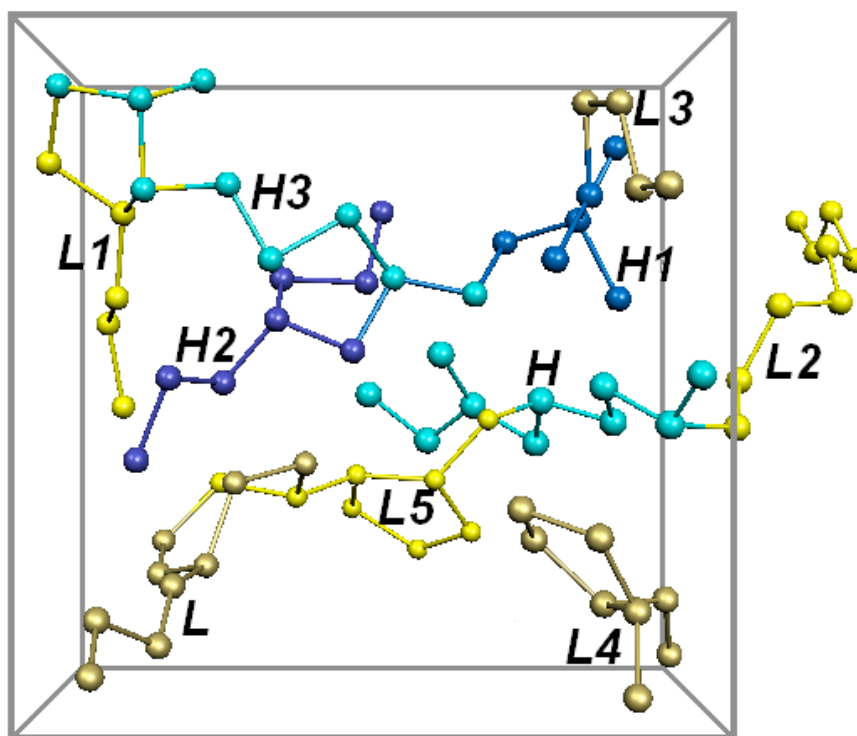
Figure 3.11: 4 valence states and 5 conduction states of model M_1.

In the figure, "H" symbols "HOMO" state; "H1" is short for the first state lower than the "HOMO", and so on; "L" symbols "LUMO" state and "L1" the first state higher than the "LUMO", and so on. To help understand the figure accurately, we point out here that for each state, only the atoms possessing the most (a dominant percentage) charge are shown in the figure. The percentage of the charge varies approximately from 70 to 95%, but never reaches 100%. If 100% charge indeed was shown, then all atoms would have been included and it would not be as revealing.

Also this is contrary to a perfect crystalline network, in which all atoms approximately carry the very same amount of charge. No particular subgroup can then be extracted.

State #1024(-0.34eV, a valence state) and state #1025(0.34eV, a conduction state) of model M_1 are shown again in Fig. 3.12 along with the filaments from the other 6 models. For model M_2-M_7 only one most localized state is shown. Again, a dominant amount of charge is included for each state, and the amount varies slightly between the models to manifest the filaments. For all these models, more than one localized states also form filament-like structures in general. The strength of the effect varies slightly among the models.

It is natural to connect these filaments to the topological-electronic correlation previously discussed. For model M_1, which is a typical example, when examined closely, the electronic filament from state #1024 (a valence tail state) has both short bonds and small bond angles along the chain, while #1025 (a conduction tail state) has both long bonds and large bond angles along the chain. In a way, the electronic filaments appear to be sitting at the very center of the topological-electronic correlation.

3.3.4   Overlap between filaments

We know that the electronic structure is directly derived from the topology of the network, and thus the topological filaments might be the centers for the electronic filaments to appear. Indeed we observe large correlation between the electronic fila-
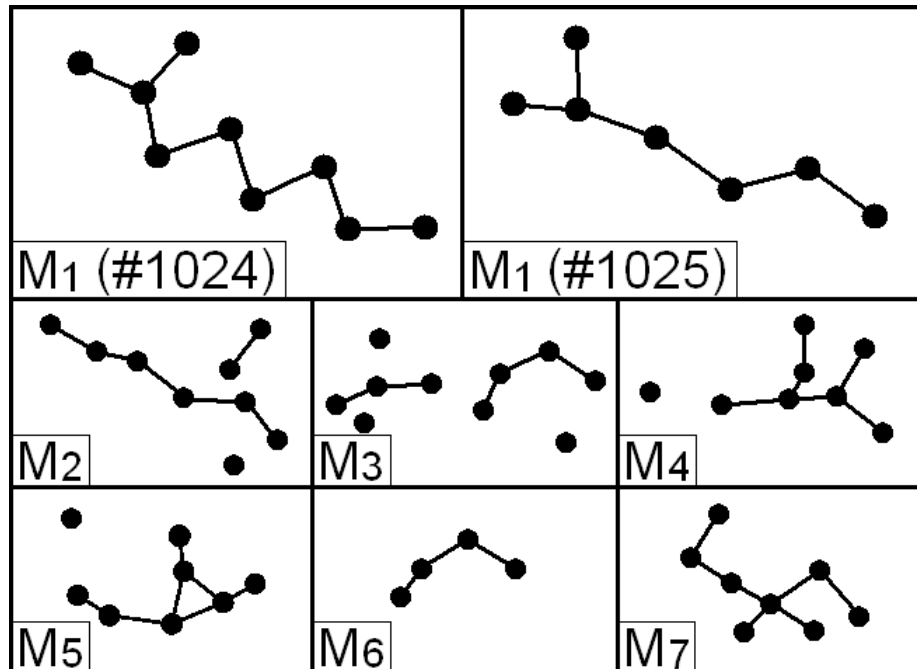
Figure 3.12: The filamentary charge path of 7 models. For Model M_1, two states are shown. For M_2-M_7 only one most localized state is shown.

ments and the topological filaments. Figure. 3.13 is an illustration of this connection between the short-bond clusters and the most localized state ((H)OMO state) for the M_1 model. Cyan atoms denote the 1% shortest bonds and their direct neighboring atoms. Yellow and gold atoms denotes the 95% charge of the state #1024 (H). Gold atoms denotes the overlapping atoms with the shortest bonds atoms and their direct neighboring atoms. (This is not exactly the topological filaments since we have included the nearest neighbors too. But this is a demonstration that the electronic filaments locate inside the vicinity of the topological filaments.) The overlap is visibly large. The picture is similar for state H_1, H_2 and next a few states, although,

the general trend is, the less localized the state, the less overlap we have with the topological filaments.
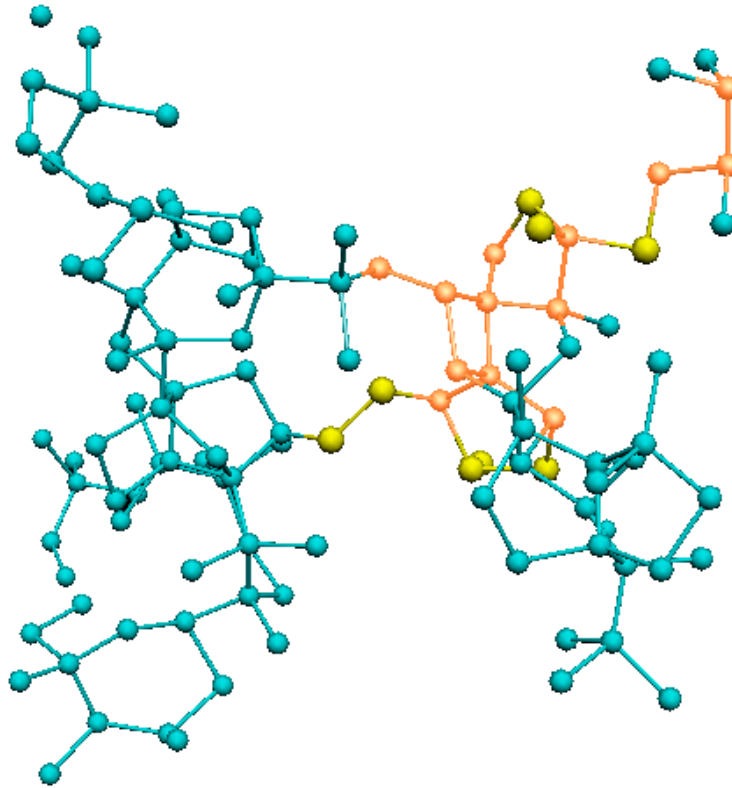
Figure 3.13: Topology-Electron correlations. The overlapping (gold) between short bonds (gold and cyan) and large charge (gold and yellow) of state #1024 of M_1 is shown.

A closer inspection, however, reveals the overlapping is not as ideal as we expected. In the figure we see there is non-overlap part. This also happens for state H1, H2 and so on, and the other side of the gap, the conduction states as well (overlap to the long bond filaments). The exact mechanism of how these two types of filaments overlap is still a puzzle.

3.3.5   Discussion

Here we offer a heuristic explanation of our observation that valence tail states are preferentially localized on short bonds and conduction tail states localized on long bonds. Short bond length has two consequences: (1) it will increase the transition integral; the energy of valence band states are lowered while the energy of conduction states is lifted relative to a hypothetical reference crystal (diamond for a-Si); (2) Small bond lengths increase the charge at the center of the bonds (states near valence edge). Thus if we make the significant assumption that the valence and conduction tails should be associated with either short or long bonds, it is clear that the electronic (band-energy) is optimized if the valence tails are associated with short bonds, and the long bonds would "do the least damage" if put above the Fermi-level, or linked with the conduction tail. This completely neglects other contributions to the total energy, though the observation of the effect in density functional calculations suggests that the band energy *is* the key term.

3.3.6   Section summary

We have discovered a model-independent feature of the electronic structure of a-Si, namely the electron-topology correlation. This correlation is especially strong for band tail states, where valence tail states are correlated to short bond (small bond-angle) in space and conduction tail states correlated to long bond (large bond-angle).

Filamentary electronic paths (electronic filaments) characterize this electron-topology correlation for very localized states.

3.4 Topology-Urbach correlation

3.4.1 The conjecture

From our observations, the topological correlation (filament) stands as the origin of the electron-topology correlation characterizing the band tail states in amorphous silicon. We now bring up our conjecture that the topological correlation (filament) sits at the very root of the Urbach tail.

Firstly we show that any relaxation process leads to topological correlation (topological filaments). We have examined 9 of our well relaxed a-Si models and have always found topological filaments (TF). Further, we intentionally removed atoms from a perfect crystalline Si network (to be mentioned in more details) and the relaxation of these point-like defects leads to clear 1-D filament-like local topologies. In a different relaxed system, amorphous SiO_2, we also found bond correlations. It is more cluster-like than filament-like due to the floppier bonding of SiO_2. In our understanding, unlike SiO_2, a-Si's covalent structure being rigid (especially along the bond-angles) is the reason the topological correlations appear more in 1-D filament-like shapes: apparently for such systems strain is preferentially relaxed along filamentary paths.

Secondly, our relaxed models universally exhibit Urbach tails. In our model M_1 (a DTW 512 a-Si model), exponential decay is evident with an Urbach energy of 107meV (Fig. 3.14). It is interesting that a clear signature of exponential tailing is seen even with a 512-atom model. We have also used maximum-entropy techniques to extend such calculations to high-quality 10^5 atom a-Si models, and such calculations reveal good quality exponential tails without exceptions.

To further examine our suspicion that topological correlation (filament) is responsible for the Urbach tails, we did two types of tests. In the first, we begin with a 512-atom model of Si in the diamond (crystalline) structure, and create two vacancies. We then relax the network to a local energy minimum with small forces. Before the relaxation, the model exhibits a sharp band edge like the ideal crystal, with gap states arising from the vacancies. Relaxation involves many atoms. Analysis of the post-relaxation pattern in our network shows that the deviation from ideal crystalline symmetry appears to be largest along 1-D filaments beginning at the site of the defects, decaying into space. This appears to be the simplest form of our topological filaments. As we illustrate in Figure 3.14, interestingly, this relaxation leads to an exponential valence tails in the DOS. It is worthwhile to mention that recent ion bombardment experiments reported the appearance of an Urbach tail well before amorphization, with a characteristic Urbach energy varying in the range 280-370meV for Si (compared with 350meV for our relaxed vacancy model).
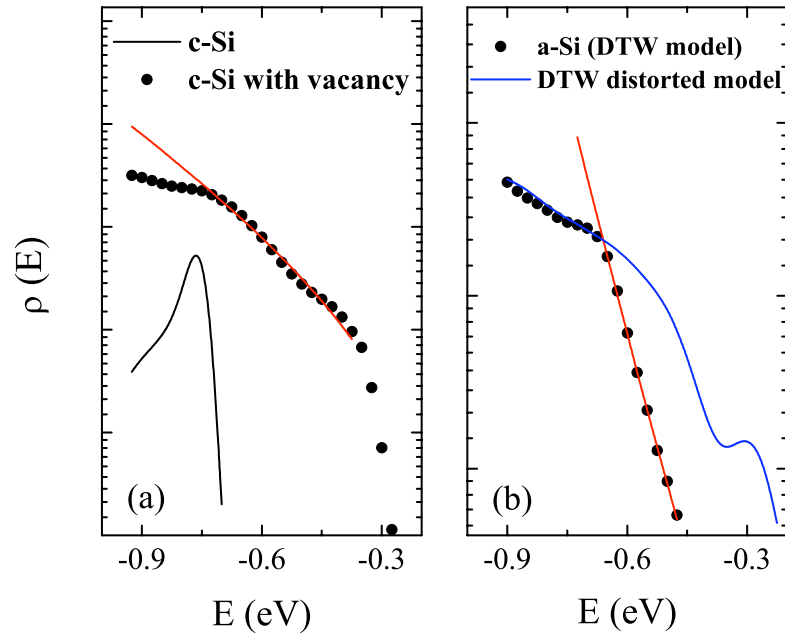
Figure 3.14: Valence band tails for crystalline Si and Crystal Si with two vacancies.

In the second type of tests, we start out from a good a-Si model (we applied this procedure on 64, 216 atom a-Si models, which manifest more primitive yet visible exponential tails), and distort the topological filaments by randomly shortening or lengthening the bond lengths in the filaments, by small magnitudes. In this way, we do not create further defects, and the overall structure of the network still remains somehow close to the original network. The resulting density of states of this 'distorted' model has the band tails that extend clearly further into the gap and deform into non-exponential decays. Figure 3.14 shows the valence tail of the original DTW model and the 'distorted' model. While the relaxed DTW models shows

a clear exponential tail with Urbach energy of 107meV, the distortion in the bond lengths has modified the functional form of the tail from exponential to something more Gaussian. This effect repeats in our tests.

3.4.2 Discussion

With the first kind of tests, we show that even the simplest topological filaments lead to exponential decay (Urbach tail). In the second kind of tests, we show that without the topological filament, exponential decays disappear. So far, we come to infer that the Urbach edges in a-Si come from the topological filaments. We understand that our study is more experimental than rigorous. There still might be other unknown factors involved. And the analytical form between the topological correlation and the Urbach tail is not possible at the moment. Nevertheless, we think it is a reasonable inference that the topological filaments play an essential role in Urbach tailing effect in systems like a-Si.

The meaning of topological filaments and electronic filaments emerges as the follows. We found that these two kind of filaments strongly overlap at the states near the band edges where electronic filaments appear. Optical and conductivity measurements are determined primarily by the character of the electron states near the Fermi level, and this is true also for lightly doped materials. Thus, our demonstrated correlation between EF and TF may be interpreted as a link between transport properties and the TF present in a-Si. We have already shown elsewhere that localized and

partly-localized deep tail states always have a strong electron-phonon coupling[50]; this inference goes a step further and shows that rather simple 1-D structures are at the root of this large coupling. If one considers the Kubo formula[2], the conductivity is expressible as a sum over transitions between occupied and unoccupied states: transitions between short-bond and long bond filaments, both with energies specially susceptible to phonons[50]. Hence, one envisions carrier transport as a phonon-driven process among EF. As the TF (correlated with the EF) exhibit distinct structural signatures, the very phonon modes that enhance the transport are determined in part by the TF.

Recent experiments in the area of cuprate superconductivity employing atomic-resolution tunnelling-asymmetry imaging reveal complex patterns associated with strong uniaxial "stripe" disorder of the tetragonal basal plane[51], as well as patchy disorder associated with superconductive and pseudogaps[52]. The latter could create filamentary Urbach tail states which could couple to interlayer dopant charges to form a dopant-based network, as suggested by Phillips[53]. While there are obviously stark differences between the cuprates and a-Si, the similarity of the topology of the TF/EF and the STM images is of interest. Finally, we have noted elsewhere that qualitative features of the states near the gap reveal universality. As eigenenergy is varied from midgap into a mobility edge, the qualitative evolution of the structure of the states is identical for Anderson models, realistic structural models as discussed here, and even lattice vibrations with mass and spring constant disorder[11]. While

the origin of the pseudogap in the cuprates is quite different from the optical gap in a-Si, the similarity in the topology of the states seen in Ref. [51] and our work hints at the possible existence of TF in the cuprates as well.

3.4.3   Section summary

We show that the existence of the topological filaments leads to Urbach tail. We point out that topological filaments appears in all of our relaxed amorphous networks, and Urbach tail appears for all these models. We show that even with the simplest type of topological filament (a chain from a relaxation of point-like defects in a crystal) Urbach tail shows up. We also show that with small amount of tampering with the topological filaments, the Urbach decay is severely altered into non-exponential form. With these evidences we come to the inference that the topological filaments stand at the heart of the universal Urbach tails.

3.5   Chapter conclusion

We have discovered significant and reasonably model-independent features of the network and electronic structure of a-Si, namely the topological correlation (TF) and the electron-topology correlation (EF) as presented in section 3.2 and section 3.3 of this chapter. Significant overlap between the two is revealed for band tail states. In section 3.4 we subsequently point out that the existence of the topological filaments leads to Urbach tail. We show that topological filaments and the Urbach tail are

mutually correlated. In various cases we prove that they always appear or disappear simultaneously. These arguments are still non-conclusive but we think they are steps toward the center of Urbach tail problem. Meanwhile filament-like topologies are reported to be observed in very different systems. With our evidences, we think it is a reasonable inference that the topological filaments sit at the origin of Urbach tailing effect in systems like a-Si.

CHAPTER 4

A semi-quantitative scattering theory of amorphous materials

The content and results presented in this chapter are submitted: Mingliang Zhang, Yue Pan, F. Inam and D. A. Drabold, Phys. Rev. Lett. (5/2008). [54].

4.1   Overview

Electronic localization induced by diagonal disorder or by structural disorder has been intensively studied over nearly fifty years[55]. However, key properties like the energy dependence of the Inverse Participation Ratio (IPR), the location of the mobility edges and Urbach energy are expressed in an obscure way, not directly accessible to experiment or simulation[8, 9]. Perturbation theory has been applied to estimate the electron states of amorphous solids (AS) starting with a crystalline counterpart as zero order solution[56] even before Anderson's classical work[8, 9]. In this chapter we suggest that a local formulation of perturbation theory is effective for the localized states confined to one distorted region. Also for the first time we relate important physical quantities of the location of the mobility edge, Urbach decay rate (Urbach energy) and energy dependence of IPR etc. to basic network properties.

4.2   Localization criterion

Similar to the theory of elasticity[57], the distorted regions in AS can be characterized by local strains referring to their local reference crystal (LRC) and local rotations. By a suitable choice of origin and orientation of LRC, the atomic displacements of a distorted region of AS relative to its LRC are small. Thus the relative change in potential energy for each distorted region in AS is small. Perturbation theory is justified for each distorted region. The semi-classical approximation (SCA)[58] can further simplify the calculation of scattering waves caused by a distorted region, since the de Broglie wavelength for low-lying excitations is of order one bond length ($\approx$2.35 Å in a-Si[59]), a distance much shorter than the characteristic range in which the random potential fluctuates[18, 19]. The motion of electronic packet under extra force of AS relative to LRC can be described by the Ehrenfest theorem[58].

We first formulate an intuitive localization criterion for the states confined to one distorted region. Then the IPR, the position of mobility edge and Urbach energy are related to the distortion relative to the LRC, the coordination number and the inter-cell transition integral. The predictions are consistent with available experiments. We also performed *ab initio* local density approximation (LDA)[15] and tight binding approximation (TBA)[60, 11] computations on a-Si to verify our results.

Consider a distorted region $\mathcal{D}$, with linear size L. Using the primitive cell of LRC numbering the atoms in $\mathcal{D}$, the x-component of extra force suffered by an

electron relative to that of LRC is

$$F_x(\mathbf{r}) = \sum_{\mathbf{n}\beta} \frac{\partial^2 U(\mathbf{r} - \mathbf{R_n})}{\partial R_{\mathbf{n}x}\partial R_{\mathbf{n}\beta}} u_{\mathbf{n}\beta}^s, \beta = x, y, z \tag{4.1}$$

later its characteristic value of is denoted as F. $\mathbf{n}$ is lattice index, $\mathbf{R_n}$ and $u_{\mathbf{n}\beta}^s$ are the position vector and the βth component of the static displacement of the atom $\mathbf{n}$ respectively. $U(\mathbf{r} - \mathbf{R_n})$ is the potential energy felt by an electron at $\mathbf{r}$ from the atom at $\mathbf{R_n}$.

A Bloch wave $\psi_{n\mathbf{k}}^c$ of LRC passes through $\mathcal{D}$, and in SCA[58], the change in the x component of the wave vector after scattering is

$$\Delta k_x \sim \frac{(FL)_x}{\nabla_{k_x} E_{n\mathbf{k}}} \tag{4.2}$$

FL measures the magnitude of random potential in $\mathcal{D}$. The phase shift $\delta_{n\mathbf{k}}$ of state $\psi_{n\mathbf{k}}^c$ is determined by the change in momentum and the propagation path of the Bloch wave

$$\delta_{n\mathbf{k}} \sim \frac{FL^2}{|\nabla_{\mathbf{k}} E_{n\mathbf{k}}|} \tag{4.3}$$

where $E_{n\mathbf{k}}$ is dispersion relation of the nth energy band of the LRC. FL^2 is the strength of a potential well (the product of the depth of potential well and the range of force) in standard scattering theory[61]. If the first coordination shell around an atom is spherically symmetric, the dispersion relation in TBA is[61]

$$E_{n\mathbf{k}} \sim E_{n0} - zI_n \cos k_x a \tag{4.4}$$

E_{n0} is the middle of the nth band $(k_x a = \pi/2)$, z is the coordination number of a cell, I_n is the transition integral for the nth band, a is the lattice constant in LRC. For

a semi-quantitative discussion, crude dispersion relation (4.4) will not invalidate any essential points. If the phase shift $\delta_{n\mathbf{k}}$ of the secondary scattering waves relative to the primary wave is $\sim \pi$, then outside $\mathcal{D}$, scattering waves will interfere destructively with the primary Bloch state. No probability amplitude appears outside $\mathcal{D}$. A localized state is therefore formed inside $\mathcal{D}$ due to the constructive interference of a Bloch state $\psi_{n\mathbf{k}}^c$ and its secondary scattering waves.

4.3 Mobility edges

Bloch states of LRC at top of valence and at bottom of the conduction edges are susceptible to the random potential. The former is a shorter wave, sensitive to details of atomic displacements of a distorted region. The latter is a long wave, a small random potential will easily produce a change in momentum comparable to $\hbar\mathbf{k}$ itself. In other words, states with small group velocity are easily localized. The group velocity of an electron in state $\psi_{n\mathbf{k}}^c$ in TBA is $v_{n\mathbf{k}}^g \sim \frac{zI_n a}{\hbar}\sin k_x a$, states near to bottom ($k_x a \sim 0$) and states near to top ($k_x a \sim \pi$) have small $v_{n\mathbf{k}}^g$. According to Eq. (4.3), they are more easily localized than the states in the middle of a band for a given random potential. For k close to $\frac{\pi}{a}$, with TBA dispersion relation (4.4), group velocity of state ψ_k^v is $v_k^g = \frac{Iz}{\hbar}(\frac{E_0-E}{Iz})^{1/2}$, $E_0 = E_0^V + zI_V$ is the top of the valence band. By Eq. (4.3), under TBA, for a valence state ψ_k^v with energy E_k, the change in phase shift with energy is according to $\frac{d\delta_k}{dE} = \frac{FL^2}{a(E_0-E_k)^{3/2}(Iz)^{1/2}}$. For a given distorted region, Bloch states close to E_0 will suffer larger phase shift. They are more readily

localized than the states in the middle of the band. Similar conclusion holds for the Bloch states in the bottom of conduction band. In Fig. 4.1 the IPR is plotted against electron energy for a-Si512. Large IPR appears at the edges of a band, in agreement with the above prediction.

The upper mobility edge of the valence band is the deepest energy level $E_{\mathbf{k}_*^V}^V$ that the largest distorted region could localize, i.e. produce a phase shift π for the corresponding Bloch state. In TBA, this leads to $\sin k_*^V a = \frac{FL^2}{zI^V a\pi}$. The energy difference between the top of a band and the mobility edge is $E_{me}^V = z_V I^V \{1 - [1 - (\frac{FL^2}{z_V I^V a\pi})^2]^{1/2}\} \sim \frac{(\frac{FL^2}{a\pi})^2}{z_V I^V}$, last $\sim$ only holds for $\frac{FL^2}{z_V I^V a\pi} << 1$. It is obvious that stronger random potential and narrower band leading to a deeper mobility edge. The lower mobility edge of the conduction band can be obtained similarly. The energy difference Δ_m between the lower mobility edge of the conduction band and the upper edge of the valence band is

$$\Delta_m \approx G^C + [\frac{(\frac{FL^2}{a\pi})^2}{z_V I^V} + \frac{(\frac{F_C L_C^2}{a_C \pi})^2}{z_C I^C}] \tag{4.5}$$

where G^C is the band gap of LRC. Because van Hove singularity is smeared out in AS, gap in amorphous solid is ambiguous. Δ_m can be defined in a simulation by identifying two edge states.

In the middle of a band $k_x a = \frac{\pi}{2}$, the group velocity reaches its maximum $\frac{zI_n a}{\hbar}$. By Eq. (4.3), to localize the states in the middle of the nth band, we need $\frac{FL}{zI_n} \frac{L}{a} \gtrsim \pi$. States in the middle of a band are most difficult to localize. If those states are localized, the whole band is localized. A stronger localization condition is $\Delta k \sim k$.

In the middle of band $k_x = \frac{\pi}{2}\frac{1}{a}$, by Eq. (4.2) the change in wave vector is $\frac{FL}{zI_n a}$. It leads to the condition to localize a whole band $\frac{FL}{zI_n} \gtrsim \frac{\pi}{2}$, is smaller than $\frac{FL}{zI_n} \sim 6-34$[62]. The deeper localized states in AS are generated by the deeper Bloch states of LRC, are spread in several distorted regions. Because current local description only considers the states localized in one distorted region, we cannot expect a better estimation.

4.4   IPR relation

The IPR I_j of a localized eigen state ψ_j could be approximated as[55] $I_j \sim \frac{a^3}{\xi_j^3}$, ξ_j is the localization length of ψ_j. If a Bloch wave $\psi_{n\mathbf{k}}^c$ suffers a phase shift π by some distorted region to produce ψ_j, it is localized in range $\xi_j : \xi_j \Delta k \sim \pi$. The change in wave vector is $\Delta \mathbf{k} \sim \frac{FL}{\nabla_{\mathbf{k}} E_{\mathbf{k}}}$,

$$\xi_j \sim \frac{\pi}{\Delta k} = \frac{\pi \nabla_k E_k}{FL} \sim \frac{\pi z I_n a \sin ka}{FL} \qquad (4.6)$$

$\sim$ is obtained under TBA. According to Eq. (4.1), $F \sim \epsilon$, ϵ is the relative change in lattice constant. To minimize the free energy, a denser region with shorter bonds and small angles will gradually decay away toward the mean density rather than exhibit an abrupt transit to a diluter region and *vice versa*. Therefore the size L of a denser distorted region is proportional to ϵ. Eq. (4.6) indicates $\xi \sim \frac{a}{\epsilon^2}$[56]. The advantage of Eq. (4.6) is that it reveals the role of the coordination number z and the transition integral I. The dependence on $\mathbf{k}$ (wave length and propagation direction of Bloch

wave) is also displayed in Eq. (4.6): close to band edge of LRC, $ka \sim 0$ or $\frac{\pi}{a}$, the localization length is small and IPR is high (see Fig. 4.1).

Making use of Eqs. (4.6) and (4.4),

$$\xi_j(E_{kj}) = \frac{\pi z I_V a}{FL}[1 - (\frac{E_{kj} - b_{me}^V + z I_V - E_{me}^V}{I_V z})^2]^{1/2} \tag{4.7}$$

b_{me}^V is the location of the mobility edge of valence band. When we approach b_{me}^V from the upper side with higher energy, it is easy to find $\xi_j \to L$ from Eq. (4.7), localization length ξ approach to the size L of whole sample as $(E_{kj} - b_{me}^V)^\alpha$, where $\frac{1}{2} < \alpha < 1$, it is close the lower bound of previous works[63]. The trend expressed by (4.7) is consistent with a simulation based upon time-dependent Schrodinger equation[64].

For a localized state derived from Bloch wave ψ_{kj}^c in LRC, the energy dependence of IPR can be found

$$I(E_{kj}) \sim \frac{(FL/\pi z I_V)^3}{[1 - (\frac{E_{kj} - E_0^V}{z I_V})^2]^{3/2}} \tag{4.8}$$

This is a new prediction of our work. Eqs. (4.7) and (4.8) are not quite satisfied because E_{kj} is the corresponding energy level in LRC, not the eigenvalue of the localized state ψ_j^a. It can be cured by taking into account energy level shift caused by the disorder in AS relative to LRC. Fig. 4.1 shows IPR vs. eigenvalues in a 512-atom model of a-Si[18]. As expected from Eq. (4.8), IPR decreases from highest values from band edges towards inside of a band. The functional form (4.8) fits the simulation rather well.
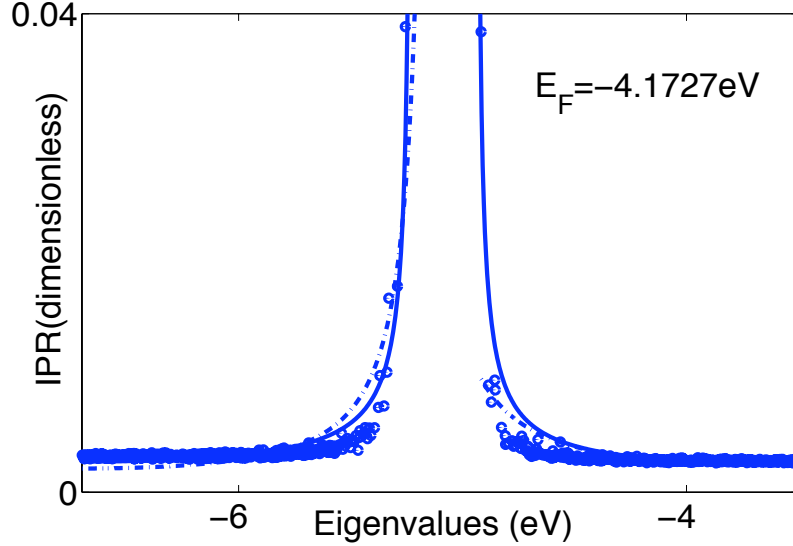
Figure 4.1: IPR of 512-atom model of a-Si, dots from *ab initio* calculation[15], dashed line and solid line are from two parameter (FL and zI) least squares fit and eye guide fit with Eq. (4.8).

According to Eq. (4.8), the least squares fitting parameters in Fig. 4.1 are $(FL)_V = 1.256$eV, $(zI)_V = 3.185$eV, $E_0^V = -7.390$eV, $(FL)_C = 1.437$eV, $(zI)_C = 3.502$eV, $E_0^C = -1.080$eV. The width of valence band of c-Si is about 2.7eV, the width of conduction band is about 2.3eV[65]. The fit parameters are reasonable-something like what we expect for Si. Gap for c-Si is 1.12eV[65], using above parameters with help of Eq. (4.5), the distance between mobility edges is 2.205eV. Result from LRC model falls in the range 1.58-2.43 eV of the observed optical gap[66, 67, 68].

In a distorted region of a-Si where bonds are shortened, valence states have more amplitude in the middle of bonds. Random potential $V_a - V_c$ (the difference between the amorphous and crystalline potentials) is important only in the middle

of bonds rather than close to the core of atoms. Electrons will feel $V_a - V_c$ more than a region where bonds more close normal. Valence tail states are easier localized in a distorted region with shorter bonds[18, 10]. On the other hand, in a distorted region with longer bonds, the conduction levels are lowered and the probability of conduction electrons staying in the middle of nearest neighbor atoms becomes larger than a region where bonds are closer to the mean. Conduction tail states are more readily localized in a distorted region with longer bonds and large angles[18, 10].

4.5 Urbach decay-rate relation

The effect of three- and four- points correlation on the shape of band tail is subtle, localized states adhere to 1D filaments in AS network[19]. In the spirit of scattering theory of line shape[69], Urbach energy can be assumed as coming from the relative shift of energy levels of LRC. Suppose Δb is the distribution width of bond length (BL), the blurring δk in wave vector k is $\frac{\Delta b}{b}k$. The shift of level E_k^v (E_k^c) for a Bloch state ψ_k^v (ψ_k^c) in valence (conduction) band by the disorder in AS is $\Delta E_k^{v(c)} = \int d\tau (V_a - V_c)|\psi_k^{v(c)}|^2$. The relative level shift due to this BL distribution is $\delta k \frac{d}{dk}\Delta E_k^c$. It is easy to see $V_a - V_c \propto \frac{\Delta a}{a}V_c$. Then the Urbach energy is

$$E_U^{V(C)} \sim \frac{\Delta b}{b}k \cdot \frac{1}{k}\frac{\Delta b}{b}V_c = (\frac{\Delta b}{b})^2|V_c| = \frac{(\frac{\Delta b}{b}|V_c|)^2}{|V_c|} \tag{4.9}$$

If we make a correspondence between structural disorder $\frac{\Delta b}{b}|V_c|$ and on-site spread W of levels, Eq. (4.9) is comparable to $E_U \sim 0.5\frac{W^2}{B}$ (B is the band width) [70] and $E_U \sim$

$\frac{\pi}{4}\frac{W^2}{3\pi^2\frac{\hbar^2}{2mL^2}}$ [71], where L and W are correlation length and variance of random potential. Eq. (4.9) is also consistent with an assumption of Cody et. al. to explain their absorption edge data in a-Si:H[72]. By notice the width of BL distribution is $\frac{\Delta b}{b}\approx 0.1$ and $|V_c|\sim 1-10$eV, the order of magnitude of mobility edge should be $(\frac{\Delta b}{b})|V_c|$, several tenth eV to 1eV. Urbach energy is around several tens to several hundred meV. Both agree with experimental observations[73]. Eq. (4.9) indicates Urbach energy is proportional to static disorder that is characterized by $(\frac{\Delta b}{b})^2$, in consistent with the fact that Urbach energy of a-Si:H increased with deposition power[73]. Δb and b could also be explained as the width and the average value of BA distribution.

Because local compress is compensated by neighbor local tensile in AS, $E_U^V\sim\frac{\varsigma^V}{\varsigma^C}E_U^C$, where ς^V (ς^C) is an order one dimensionless constant characterizing the peak (node) of valence (conduction) states. In a-Si and a-Si:H, random potential (V_a-V_c) has larger distortion in the middle of Si-Si bonds, since valence states are more in the middle of bonds than conduction states[59], they feel the distortion more. Therefore $\varsigma^V>\varsigma^C$. One expect $E_U^V>E_U^C$. This agrees with measurements in a-Si:H: $E_U^V\sim$43-103meV vs. $E_U^C\sim$27-37 meV, linear relation among E_U^V and E_U^C has also been observed[73].

To test correctness of Eq. (4.9), we finished a TBA calculation for DOS of six a-Si models with 20,000 atoms[60, 11, 74]. Urbach energies, the width $\sigma_{\cos\theta}$ of BA distributions and the width Δb of BL distribution are extracted. Fig. 4.2 clearly shows good linear relation between E_U^V (E_U^C) and $\sigma_{\cos\theta}^2$, curves pass origin (Urbach
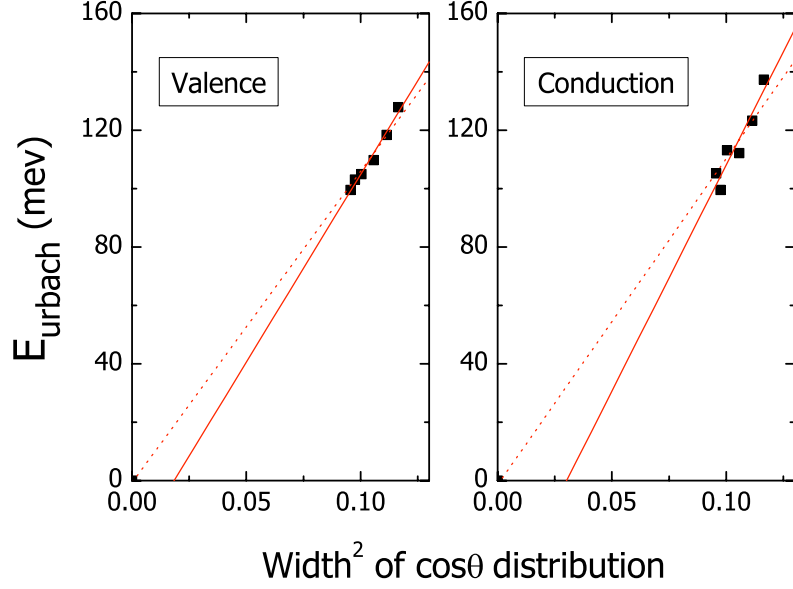
Figure 4.2: E_U^V and E_U^C vs. $\sigma_{cos\theta}^2$: 6 squares are extracted from TBA calculation, dotted line and solid line are least square fits with and without (0,0) points.

energy is zero for crystal) as displayed in Eq. (4.9). It can be further tested in ion implanted samples, where a continuous increase disorder from crystal to amorphous are realized by increasing the dose[75]. The E_U^V (E_U^C) vs. $(\Delta b)^2$ curve does not pass origin (not showing here), this is an indication that BA disorder is a little more decisive in determine the shape of a band tail than BL disorder for a well relaxed structure[18, 10].

The electron-phonon interaction is strong in AS[50]. At finite temperature, the displacement of an atom in AS deviate from the position in the LRC at zero temperature is a vector sum of the static displacement $\mathbf{u}_s$ and thermal vibration

displacement $\mathbf{u}_T(t)$ from the zero temperature configuration of AS, t is the time moment. In ordinary absorption experiment, time interval T is much longer than the period of the slowest mode, therefore $\overline{E_U^C} = \frac{1}{T}\int_0^T dt \varsigma^C(\frac{\mathbf{u}_s + \mathbf{u}_T(t)}{a})^2|V_c|$. Atoms vibrate around their equilibrium points in AS, the time average of the cross term $\mathbf{u}_s \cdot \mathbf{u}_T(t)$ is zero. Thus Urbach energy from static disorder and from thermal disorder is additive[72] $\overline{E_U^C} = E_{Us}^C + E_{UT}^C$, $E_{Us}^C = \varsigma^C(\frac{u_s}{a})^2|V_c|$. Thermal part $E_{UT}^C = \varsigma^C\frac{\overline{\mathbf{u}_T^2}}{a^2}|V_c|$, $\overline{\mathbf{u}_T^2} = \frac{1}{T}\int_0^T dt[\mathbf{u}_T(t)]^2$ is the long time average of the square of amplitude of vibration. An ultra-fast probe of absorption edge may find oscillating in $\overline{E_U^C}$. Since $\overline{\mathbf{u}_T^2} \propto \frac{k_B T}{B_C}a^2$[61], B_C is binding energy in the diluter regions where conduction tail states are localized, $E_{UT}^C = \varsigma^C k_B T \frac{|V_c|}{B_C}$. $\overline{E_U^C}$ linearly increases with temperature. Similarly result holds for $\overline{E_U^V}$. The is consistent with the fact that above 350K absorption edge linearly increase with $k_B T$ in a-Si:H[76, 12]. Because $B_V > B_C$, E_U^C is more susceptible to thermal disorder than E_U^V[77], as observed in ref. [12].

4.6   Summary

For *realistic* amorphous solid with *topological disorder*, by viewing an AS as many distorted regions relative to corresponding LRC, we push forward essential understanding on localized states confined in one distorted region. The predicted IPR, mobility edge, the dependence on static disorder and on temperature of Urbach energy agree with available experiments and simulations. We explained the fact that valence tail states are more localized in a denser region with smaller BA and shorter

BL and conduction tail states are more localized in diluter region with longer BL and larger BA in a-Si[18, 10]. Localized states in several distorted regions and other problems involving global topology will be addressed in future.

CHAPTER 5

Study of Boron Doping

5.1 Overview

It is known that the doping efficiency of B in a-Si:H is very low. It is around ten percent at low concentrations [78, 49] and falls off to less than one percent as the concentration increases. This is in strong contrast to the situation for c-Si, where the doping efficiency is virtually one hundred percent.

Spear and LeComber reported that a-Si:H could be doped either p or n type by the addition of boron or phosphorus[5]. This first observation of electronic doping in an amorphous semiconductor set the stage for the subsequent development of a-Si:H electronic technology. Subsequent experiments confirmed that the conductivity change was due to a shift of the Fermi level. (For completeness, refer to R. A. Streets' book [5]). The behavior of B (P) doped a-Si:H very much resembles that of crystalline except for the low doping efficiency and decreased conductivity at very high B (P) concentration.

Doping in c-Si has been well explained with the effective mass theory[5, 6], where B is expected to ideally substitute a Si and is bonded to four Si neighbors. The observation of effective doping of B (P) in a-Si:H is significant because of the theoretical prediction that substitutional doping of an amorphous semiconductor is impos-

sible, described as follows. In covalent amorphous solid, the bonding coordination Z is expected to obey the "8-N" rule[5]: $Z = 8 - N (for N \geq 4)$ and $Z = N (for N < 4)$ where N is the valence number of the element. In crystalline silicon, the periodic lattice of atoms constrains the impurity to have the same coordination as the silicon, in which case the boron or phosphorus atoms become dopant states. This topological constraint of the crystalline lattice that leads to the substitutional doping might be absent in amorphous solids.

The observation of effective doping in a-Si:H certainly contradicts this view, although the doping efficiency in a-Si:H is very low. It had long been believed that the majority of B present in a-Si:H were threefold (and therefore electrically inactive). It was J. B. Boyce and S. E. Ready[79]'s classic nuclear-magnetic-double-resonance experiment in 1988 that for the first time contradicted this belief. J. B. Boyce and S. E. Ready observed in a sample that 40 percent of the B atoms had a H atom at about 1.6 Å, very close to typical B-H distances. The exact fraction of the H that is bonded to B varied with samples but it was confirmed that a significant fraction of B having a H in the first-neighbor shell. P. A. Fedders and D. A. Drabold carried out first principle calculation[49] in 1997 and confirmed this result. The calculation indicated fourfold B was to be preferred and the conventional view was in error. H passivation was pointed out as the cause of the low B-doping efficiency. It is interesting to mention here that J. B. Boyce and S. E. Ready also observed that phosphorus behaved differently than boron in a-Si:H. The H was not directly bonded

to a measurable fraction of the P. Instead, about 53 percent of the P had an H atom at an average distance of 2.6 Å.

Another decade has now passed and the computational accuracy has been greatly improved. We now study boron doping in a-Si:H via much more sophisticated *ab initio* calculation code SIESTA 2.0 (solving the self-consistent Kohn-Sham equations with a double-zeta polarized basis for Si and H and a double-zeta basis for B). We look forward to answering following questions: (1)What are the preferred coordinations and sites for B occupation? (2)Why the low doping efficiency? (3)What happens electronically for very large B concentration?

5.2   Tetrahedral B is stable

Our MD simulation shows that tetrahedral/substitutional (fourfold) configuration of B is very stable. Various B concentrations have been tested (with or without H's presence) and the stability repeats even for high B concentration. Our result agrees with Fedders' and Drabold's calculations where fourfold boron was shown to have lower energy than threefold boron. Our result is further backed up by recent calculation from I. Santos et al.[80], which shows tetrahedral /substitutional B formation is preferred with a lower chemical potential. These results put the conventional view that non-tetrahedral B prevails in a-Si:H in error. Thus, the idea that the 8-N rule is maintained in a-Si:H appears to be incorrect.

5.3   Hydrogen Passivation

P. A. Fedders and D. A. Drabold pointed out[49] that H passivation is the main cause for low B doping efficiency in a-Si:H. They calculated averaged energies and show that a configuration of boron bonded with hydrogen has lower energy (an average energy of 0.22eV) and therefore B has higher affinity for H than Si does (an average energy of 0.44eV). Our current simulation confirms this argument. This is manifested in Figure 5.1, which are obtained via our molecular dynamic simulations. The figures demonstrate how H diffuses to form a bond with a B in the a-Si:H network at 300K. This result is typical. Our simulation always forms a B(3,1) configuration: a B bonded to three Si and one H. In our calculation the initial system with the B bonded to a Si has a free energy of -6744.44 eV. When the B is bonded to the H (bondlength ≈ 1.49Å), the system has lowered the free energy to -6752.98 eV. Please note that only energy differences are meaningful. Early experiment of J. B. Boyce and S. E. Ready[79] showed that $\frac{1}{2}$ of the borons had H neighbors about 1.4 Å away, which suggested prevailing B-H pair formation. Our result is consistent with this finding.

In Fedders' and Drabold's calculation, however, the B(3,1) formation (B bonded to three Si and one H) is found to be an effective doping configuration. They stated that B(4) (B bonded to four Si) and B(3,1) configurations both have a fourfold coordinated boron atom and both dope the material. They argued that the B-H-Si formation (B bonded to four Si and one H in between) or B-Si-H-Si formation is the
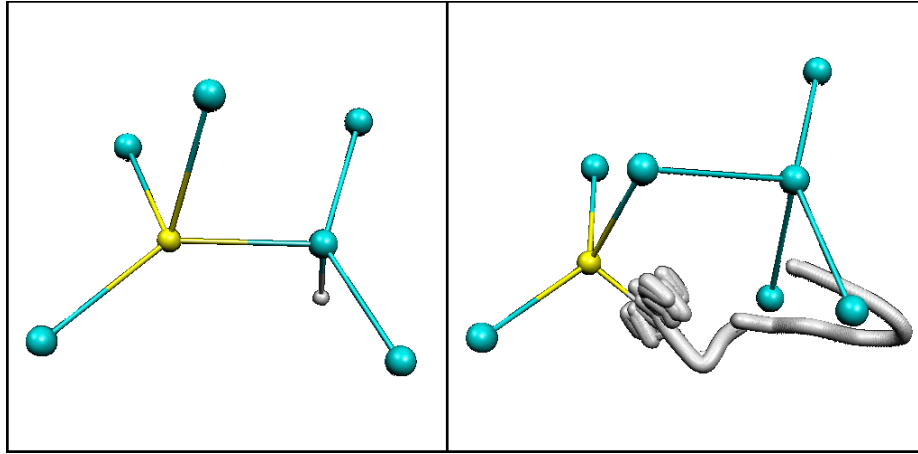
Figure 5.1: One H (white) is initially bonded with a Si atom, and is 2.83Å away from the four-coordinated B atom (left panel). After a molecular dynamic process of 0.5 ps at 300K, the H atom moves itself to bond with the B atom with a bond-length around 1.49Å. One original B-Si bond is broken and the Si shifts to bond with another Si (right panel). Therefore the B atom is still four-coordinated.

cause for non-doping, where H successfully passivates B. This is where our current result differs. Our density of state calculation reveals in Figure 5.2 that the B(3,1) formation does not dope the material. Fermi level is not shifted into the valence band within case C and D, where in either case the boron is bonded to an H atom and forms the B(3,1) formation.

While H passivation is recognized in common, our result creates a discrepancy. Does B(3,1) configuration create a dopant state or not? Our current result that the B(3,1) configuration does not dope the material can be backed up by the fact that first in Fedders' and Drabold's calculation B(3,1) has much favored energetics with an average energy of a mere 0.22 eV compared to B-H-Si's 16.27 eV and B-Si-H-Si's 16.30 eV; secondly our newer simulation forms the B(3,1) formation repeatedly and
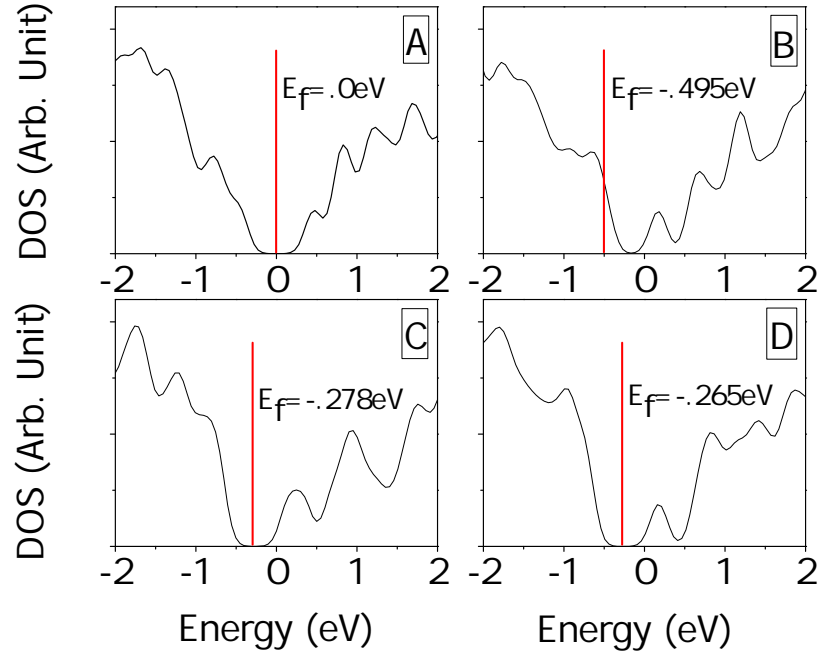
Figure 5.2: Density of states of (A) intrinsic a-Si; (B) a-Si with 1.6% B; (C) a-Si:H with 1.6%, bonded to H; (D) a-Si:H with 1.6% B, bonded to H after the MD evolution, as shown in the right panel of Fig. 5.1.

never produces the B-H-Si or the B-Si-H-Si formation. It would be hard to imagine there exists a large amount of B-H-Si or B-Si-H-Si formations in the material. B(3,1) configuration, on the other hand, can easily prevail in the network due to its favored energetics. The question becomes whether B(3,1) configuration can create a free carrier to form a dopant state. Although four-bonded, B(3,1) formation deviates from the sp3 bonding and can possibly be non-doping. The underlying mechanism, however, is unclear. If non-doping, in our speculation, both the broken symmetry from the tetrahedral formation and possible localized electron can be the cause.

5.4   High B concentration

Our calculation also finds that very high B concentration does not produce a commensurate shift in Fermi level, even without H. This can be seen in Fig. 5.3. Conductivity is not enhanced. This is consistent with earlier experiments from Tsai[81] and Leidich[82] where higher doping levels cause a large decrease in the conductivity and a corresponding increase in the activation energy. R. A. Street[5] pointed out that at these concentrations, the material is more properly described as an alloy. Therefore the network may change into an electronically and structurally different material instead of shifting the Fermi level.

5.5   Summary

Our result agrees with P. A. Fedders and D. A. Drabold's earlier theory that H passivation of B is one of the major reasons for the low B doping efficiency in a-Si:H, with the difference being whether the frequently found B(3,1) formation forms a dopant state. At the same time, our study shows that tetrahedral B formation is very stable, therefore putting the non-tetrahedral explanation in error. This coincides with the recent work from I. Santos et al[80]. Also we find that large B concentration contributes very little to the doping efficiency, whether H is included or not.

The time and amount of data involved in our Boron study was limited. More data and study are needed. We have yet to explore an potentially important category:
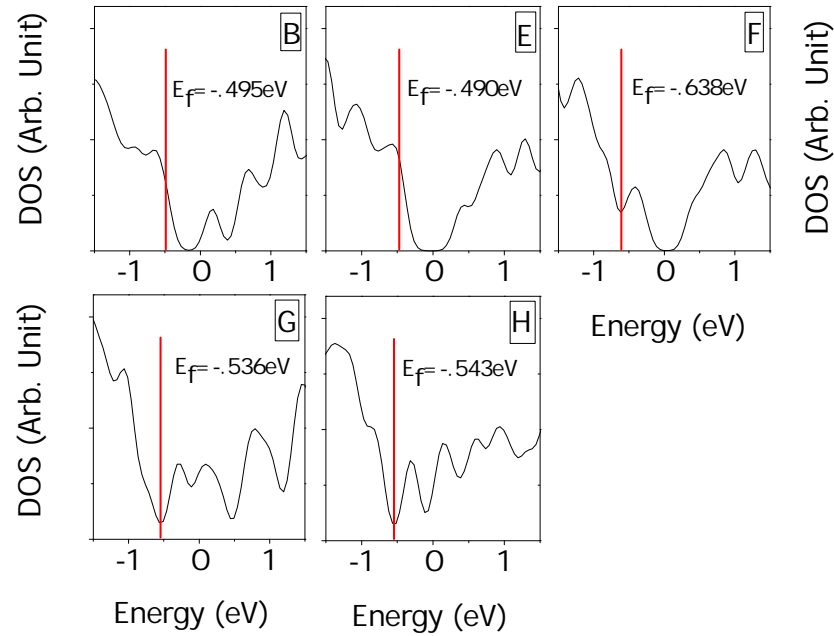
Figure 5.3: DOS and Fermi level of a-Si with boron concentration of (B)1.6% (E) 3.1% (C) 6.3% (D) 12.5% (E) 15.6%.

the localization influence on the doping efficiency. Si defects possibly induced by B have been occasionally observed and may prove revelent to many of our findings. The key list of future work regarding this topic should include: (1)further investigate B(3,1) formation and its electronic behavior; (2)monitor B-induced Si defects; study the role of localization in B doped a-Si:H; (4)calculate conductivities.

CHAPTER 6

Conclusion

6.1 What we have learned

In our study of Urbach tails, we began by searching for particular local distortions connected to the energy states in amorphous silicon. It turns out that both bond-length distortion and bond-angle distortion are correlated to the band-tail eigenstates, though the effect covers a range of distortion units instead of individual distortions. We observe that short bond and small bond angle are strongly correlated to the valence-tail states' localized charge; long bond and large bond angle are strongly correlated to the conduction tail states. These effects form an interesting asymmetry around the optical gap. The bond-length and bond angle distortions are more than local: for each state, a large set of atoms can be involved with the localized charge. For the most localized states in our a-Si models, however, these charged atoms form strong filament-like shapes. They are effectively the smallest element connecting to the localized states. In one of our papers, we reported this topology-electron correlation in detail. In addition, we also reported a topological correlation: short bond tends to stay closely with short bond and long bond tends to stay closely with long bond, regardless of electron charge. So the topology of networks forms inter-penetrating

clusters (or filaments) of short bonds or long bonds throughout the network. We call these topological filaments, resulting from the topological correlation.

In our more recent paper[19], we argued that these topological filaments stand at the heart of the Urbach tails. We show that with even the simplest topological filamentary structure (one filament form a point-like defect in a crystalline environment), we still obtain Urbach tails (exponential decaying). Meanwhile we show that with any artificial tampering of the topological filaments that our a-Si models have, the Urbach tails are strongly altered into non-exponential forms. These arguments are still non-conclusive but we think they are steps toward the center of Urbach tail problem. People observe filament-like topologies in very different systems and this boosts our confidence in recognizing topological filament as the universal feature that leads to Urbach decay.

We are only able to provide a brief and heuristic explanation why the bondlength-electron correlation exists in the way we observed. Also we showed the electronic filaments to overlap strongly with the topological filaments, and we argue that the topological filaments are the foundation of the electronic filaments and thus the formation of the eigenstates near the Fermi level. However, we are not able to explain what exact overlapping mechanism is underlying between these two kinds of filaments. Therefore, we are still far from quantitatively deriving a correlation between the topological filaments and the Urbach energy.

We find in our B doping study, that the tetrahedral formation is stable and can not be the cause for low doping efficiency. We also confirm earlier prediction by P. A. Fedders and D. A. Drabold[49] that H passivation is responsible for stopping B doping. The new issue focuses on whether B(3,1) formation creates a dopant state. Other factors we discover include that high B concentration in a-Si almost does not increase doping effect at all, a stark contrast to that of c-Si; Si defect possibly induced by B are found and may be responsible for the effect.

We successfully implemented Kubo-Greenwood formula into code SIESTA 2.0. Thermal averaging is implemented for the conductivity calculation. AC conductivity and DC conductivity calculation codes are presented. We apply AC conductivity calculation on several a-Si:H materials and have presented one of the results. We also apply DC conductivity calculation on a-Si models and crystalline Al models. The results we obtained are comparable to earlier calculation and experimental values.

6.2   Future study

We observed clear one dimensional string-like structures linking short bonds to short bonds and long to long in our continuous random network models. We have solved a few questions from a few months back. But we still haven't answered "Why does the localized electron charge tend to form filamentary shape?" and "how do electron filaments overlap with topological clusters?" . The exact structure of these filaments also needs closer inspection. The question "is the topological filament the

element correlated to the universal exponential Urbach tail?" has been answered with a "yes". Now the harder question is "how?".

We need to come up with a method of measuring the strength (length) of an electronic filaments. This quantity seems simple enough but to date we have not be able to extract it. The correlation between this length and the energy will be another interesting relation and can be revealing for the Urbach tail. The length of another filament, the topological filament, can be even more subtle to measure or extract. But to understand the overlap between the two, this work will be necessary.

Another question is at room or higher temperature, does the topological correlation decrease or increase? If regarding thermal disorder as the forces opposite to making a system stay in a metastable state, then we should expect the topological correlation to decrease, since we think of the TF as the consequence of a relaxation process. However, the higher the thermal disorder, the wider the bondlength/bondangle distributions are, and supposedly the Urbach decays extend longer indicating stronger topological correlation. These two pictures are counteractive. We will need a clear answer.

Molecular dynamic trajectories need to be inspected, with initial conditions of local vibrations in "special" parts of the network: long or short bonds. Another related perspective is the evolution of the existing defects at finite temperature. It was addressed in recent paper[39]. The question whether the defects fluctuate around some fixed points or they diffuse randomly in the network, however, still has not been

fully answered. Both the fluctuations of the defects in numbers and in spaces need to be monitored more carefully.

Future work should also involve exploring the vibrational (phonon) structure of a-Si. A correlation between the phonon states (localizations) and the topological clusters (strings) will be searched for. Phonon localization may possibly be found correlated to electronic localization too. In our investigation of topology of network and electron states, it seems only sensible to also explore the vibrational states.

Our understand of the B doping mechanism is only partial. For a more thorough picture of B doping in a-Si, we first need larger sets of data by *ab initio* calculations. H passivation is confirmed with H found to have an obvious higher affinity for B than Si does. However, the detail of H diffusion in the network is far less clear. How far can hydrogens travel in a certain time scale is unknown. Whether B(3,1) configuration create effective dopant state needs to be further investigated. H induced Si defects needs to be monitored. Furthermore and importantly, we have never had chance to study the role of localization in the low doping efficiency. The key list of future work regarding this topic should include: (1)further explore the high affinity of B for H; track the formation of H-B pairing and its structural side effects; (2)investigate B(3,1) formation and its electronic behavior; (2)investigate how localization affects B doping in a-Si:H; (3)explore the role of Si defects; (4)calculate conductivities.

Our Kubo-Greenwood formula based conductivity calculation looks promising. The next step will be more applications. The difficulty for the AC conductivity (dielectric function) test is that experimental data is lacking. Currently Dr. Mingliang Zhang of our group is working jointly on the dielectric functions with N. Podraza of electric engineering group at Penn State University. Dr. Mingliang Zhang of our group uses VASP and SIESTA AC for the dielectric function calculations. SIESTA AC results therefore will be further compared with more experimental data on the way. For the DC conductivity from SIESTA DC, we have compared our result of a-Si to earlier calculation by Tesfaye Abtew and to experimental results for c-Al. Both comparisons are very close in value. We have also applied it to B doped a-Si:H. The results are reasonable but again the lack of reference sets our limit. Both SIESTA AC and SIESTA DC's reliability needs to be further tested. Currently first principle conductivity calculation codes are not widely available. VASP offers one good option, but SIESTA AC and DC can be good alternatives. Possible future application can be on a wide variety of materials, such as various amorphous semiconductors, amorphous material with voids, molecules etc.

Bibliography

[1] F. Urbach, Phys. Rev. **92**, 1324 (1953).

[2] R. Kubo, J. Phys. Soc. Jpn. 12, 570 (1957).

[3] D. A. Greenwood, Proc. Phys. Soc. London 71, 585 (1958).

[4] R. Zallen, *The physics of amorphous solids*, Chapter 5, (p205-242), Wiley Interscience (1998).

[5] R. A. Street, *Hydrogenated amorphous silicon*, Chap 4, Cambridge Univ. Press, Cambridge UK (2002).

[6] J. M. Ziman, *Principles of the Theory of Solids.*

[7] R. M. Martin, *Electronic Structure*, Part II (p119-185), Cambridge Univ. Press, Cambridge UK (2004).

[8] P. W. Anderson, Phys. Rev. **109**, 1492 (1958).

[9] P. A. Anderson, Proc. Nat. Acad. Sci. USA **69**, No.5, 1097 (1972).

[10] J. Dong and D. A. Drabold, Phys. Rev. Lett. 80 1928 (1998).

[11] J. J. Ludlam, S. N. Taraskin, S. R. Elliott and D. A. Drabold, J. Phys. Cond. Matter 17 L321 (2005).

[12] S. Aljishi, J. D. Cohen, S. Jin and L. Key, Phys. Rev. Letter **64**, 2811 (1990).

[13] N. Bacalis, E. N. Economou and M. H. Cohen, Phys. Rev. B **37**, 2714 (1987).

[14] M. H. Cohen et al, IBM J. Res. Develop. **32**, No. 1 (1988).

[15] E. Artacho, E. Anglada, O. Dieguez, J. D. Gale, A. Garcia, J. Junquera, R. M. Martin, P. Ordejon, J. M. Pruneda, D. Sanchez-Portal and J. M. Soler, J. Phys. Condens. Matter **20**, 064208 (2008); Siesta on a-Si-512 with single zeta polarized basis sets (SZP: 1 function for 3s, 3 for 3p and 5 for 3d).

[16] Sir Nevill F. Mott, Nobel Prize Lecture (1977).

[17] G. Kresse and J. Furthmuller, Comput. Mat. Sci. **6**, 15-50 (1996).

[18] Y. Pan, M. Zhang and D. A. Drabold, *Topological and topological-electronic correlations in amorphous Si*, J. Non. Cryst. Sol. **354** 3480 (2008).

[19] Y. Pan, F. Inam, M. Zhang and D. A. Drabold, Phys. Rev. Lett. 100 206403 (2008).

[20] J. C. Phillips, Phys. Rev. B **75** (2007) 214503, and references therein.

[21] J. C. Phillips, Phil. Mag. B **79** (1999) 527.

[22] K. McElroy, J. Lee, J. A. Slezak, D.-H. Lee, H. Eisaki, S. Uchida and J. C. Davis, Science **309** (2005) 1048.

[23] St. Adams and J. Swenson, Phys. Rev. Lett. **84** (2000) 4144.

[24] S. Maslov and I. Ispolatov, Proc. Nat. Acad. USA **104** (2007) 13655.

[25] P. A. Fedders, D. A. Drabold and S. Nakhmanson, Phys. Rev. **58** , (1998) 15624.

[26] H. C. Kang, Journal of Non-Crystalline Solids **261** (2000) 169-180.

[27] T. A. Abtew, M. Zhang and D. A. Drabold, Phy. Rev. B **76** , (2007) 045212.

[28] F. Wooten, K. Winer and D. Weaire, Phys. Rev. Lett. **54** , (1990) 1392.

[29] N. Mousseau and G. T. Barkema, Phys. Rev. B **61** (2000) 1896.

[30] S. Nakhmanson, P. M. Voyles, N. Mousseau, G. Barkema and D. A. Drabold, Phys. Rev B **63** (2001) 235207.

[31] P. Biswas, R. Atta-Fynn and D. A. Drabold, Phys. Rev. B **69**, (2004) 195207.

[32] B. R. Djordjevic, M. F. Thorpe and F. Wooten, Phys. Rev. B **52**, (1995) 5685.

[33] N. Bernstein, J. L. Feldman and M. Fornari, Phys. Rev. B **74**, (2006) 205202.

[34] J. Dong and D. A. Drabold, Phys. Rev. B **54**, (1996) 10284.

[35] D. Weaire and M. F. Thorpe, Phys. Rev. B **4**, (1971) 2508.

[36] L. Colombo, Computational Material Science 12 (1998) 278.

[37] K. McElroy, J. Lee, J. A. Slezak, D.-H. Lee, H. Eisaki, S. Uchida and J. C. Davis, Science **309** (2005) 1048.

[38] C. Cohen-Tannoudji, J. Dupont-Roc and G. Grynberg, Atom-Photon Interactions, *Basic Processes and Applications*, John Wiley & Sons Inc. (1998).

[39] D. A. Drabold, T. A. Abtew, F. Inam and P. Yue, *Network structure and dynamics of hydrogenated amorphous silicon* J. Non-Cryst. **354** 2149 (2008).

[40] Panwen Shen and Yunxia Che et al., Inorganic Chemistry Series, Vol.8, Scientific publishing company, Beijing (1982).

[41] C. N. R. Rao, Transition metal oxides : crystal chemistry, phase transition, and related aspects, Washington, U.S. Govt. Print. Off., 1974.

[42] V. L. Ginzburg, and D.A. Kirzhnits, *High-temperature superconductivity*, New York : Consultants Bureau, (1982).

[43] J. B. Goodenough, Physical Review B**5**, 2764 (1972).

[44] J. Callaway, Qunatum Theory of he Solid State, Part A and Part B, Academic Press, New York (1974).

[45] P. W. Anderson, A Career in Theoretical Physics, p463, World Scientific, Singapore (1994).

[46] N. F. Mott, Metal-insulator transitions, London : Taylor & Francis (1974).

[47] A. D. Rata and T. Hibma, The European Physical Journal B **43**, 195-200 (2005).

[48] Z. Yu, M. A. Berding, R. DeWames, *Electronic structures, optical absorption, and electrical transport in VO_x*, preprint (02/2007).

[49] P. A. Fedders and D. A. Drabold, Phys. Rev. B **56** 1864 (1997).

[50] R. Atta-Fynn, P. Biswas and D. A. Drabold, Phys. Rev. B 69 254204 (2004).

[51] Y. Kohsaka, C. Taylor, K. Fujita, A. Schmidt, C. Lupien, T. Hanaguri, M. Azuma, M. Takano, H. Eisaki, H. Takagi, S. Uchida and J. C. Davis1, Science 315 1380 (2007).

[52] M. C. Boyer et al arXiv:0705.1731.

[53] J. C. Phillips, Phys. Rev. B 75 214503 (2007).

[54] Mingliang Zhang, Yue Pan and D. A. Drabold, *A semi-quantitative scattering theory of amorphous materials*, Submitted to Phys. Rev. Lett. (5/2008).

[55] B. Kramer and A. MacKinnon, Rep. Prog. Phys. **56**, 1469 (1993); P. A. Lee et al., Rev. Mod. Phys. **57**, 287 (1985); D. J. Thouless, Phys. Rep. **13**, 93 (1974).

[56] for review see K. Moorjani and C. Feldman, Rev. Mod. Phys., **36**, 1042 (1964).

[57] A. E. H. Love, A Treatise on the Mathematical Theory of Elasticity, 4th edition, Cambridge University Press (1927).

[58] A. B. Pippard, Dynamics of Conduction Electrons, New York, Gordon & Beach, (1965).

[59] W. A. Harrison, Electronic Structure and the Properties of Solids, Freeman, San Francisco, (1980).

[60] D. A. Drabold and O. F. Sankey, Phys. Rev. Lett. **70**, 3631 (1993).

[61] J. Callaway, Quantum Theory of the Solid State, Academic Press, London (1974).

[62] V. Srivastava, J. Phys.: Condens. Matter, **1**, 4311 (1989).

[63] N. F. Mott, Conduction in non-crystalline materials, 2nd ed, Oxford, Calrendon Press (1993).

[64] H. De Raedt and P. De Vries, Zeitschrift fur Physik B: Condensed Matter, **77**, 243 (1989).

[65] B. V. Zeghbroeck, http://ece-www.colorado.edu/~bart/book, Chapter 2, (2007).

[66] A. Deneuville, A. Mini and J. C. Bruyere, J. Phys. C: Solid State Phys. **14**, 4531 (1981).

[67] A. O. Kodolbas, Materials Science and Engineering B**98**, 161 (2003).

[68] K. Haga, K.Yamamoto, M. Kumano and H. Watanabe, Japn. J. Appl. Phys., Part 2, **25**, L39 (1986).

[69] for example, A. M. Stoneham, Rev. Mod. Phys. **41**, 82 (1969).

[70] S. Abe and Y. Toyozawa, J. Phys. Soc. Japan **50**, 2185 (1981).

[71] C. M. Soukoulis, M. H. Cohen and E. N. Economou, Phys. Rev. Lett. **53**, 616 (1984).

[72] G. D. Cody, T. Tiedje, B. Abeles, B. Brooks and Y. Goldstein, Phys. Rev Lett. **47**, 1480 (1981).

[73] S. Sherman, S. Wagner and R. A. Gottscho, Appl. Phys. Lett. **69**, 3242 (1996).

[74] N. Mousseau and G. T. Barkema, Phys. Rev. B **61**, 1896 (2000).

[75] for example, S. Sorieul, J.-M. Costantini, L. Gosmain, G. Calas, J.-J. Grob and L. Thomé, J. Phys.: Condens. Matter **18**, 8493 (2006).

[76] G. Weiser and H. Mell, J. Non-Cryst. Solids, **114**, 298 (1989).

[77] D. A. Drabold and P. A. Fedders, Phys. Rev. B **60**, 721 (1999).

[78] K. Winer, R. A. Street, N. M. Johnson and J. Walker, Phys. Rev. B 42 3120 (1990).

[79] J. B. Boyce and S. E. Ready, Phys. Rev. B 38 11008 (1988).

[80] I. Santos et al., In Preparation (2008).

[81] D. K. Egelsen, R. A. Street, C. C. Tsai, and J. C. Knights Phys. Rev. B, Volume: 20, Issue: 12, Pages: 4839-4846, (1979).

[82] cx D. Leidich, E Linhart, E. Niemann, et al, J. Non. Cryst. Sol., Volume: 59-6, Issue: DEC, Pages: 613-616, (1983).

[83] Glenn Elert, Val Polyakov et al.,*The Physics Factbook*^{TM}(2004).

Appendix A

Electrical conductivity calculation

A.1   Overview

T. A. Abtew[27] for the first time implemented Kubo-Greenwood formula (its dc limit form) into *ab initio* code SIESTA and dc conductivity calculation became possible. As a continuation of T. A. Abtew's work, we now implement the Kubo-Greenwood formula into the newly introduced code SIESTA 2.0. We apply our calculation on amorphous Si and metal Aluminum for dc conductivities. We compare our results to former result and relevant experimental data.

A.1.1   a-Si

T. A. Abtew applied his calculation on a-Si (64-atom model) and a-Si:H (64-atom model) models and obtained DC conductivities. We now repeat the DC conductivity calculation on a-Si with a 64 model and a 216 model at different temperatures. 1000 molecular dynamic steps are used for each temperature. The results are then thermally averaged. This averaging process is important for the thermal vibration to take effect in the conductivities. Lattice vibrations are brought into the calculation.

We did the calculation for 64 a-Si model at 300K, 500K, 700K, 1000K, 1500K and 1800K. Beside the original Fermi level, we artificially shifted the Fermi level to the left and to the right. The DC conductivities are shown in Figure A.1. From the figure we see our calculation is generating reasonable results for a-Si at different temperatures. The similarity to Abtew's work (Figure 3 in paper[27]) is clearly visible, while there is some minor difference in the values. This is understandable since the coding environment has changed and implementation details differed.
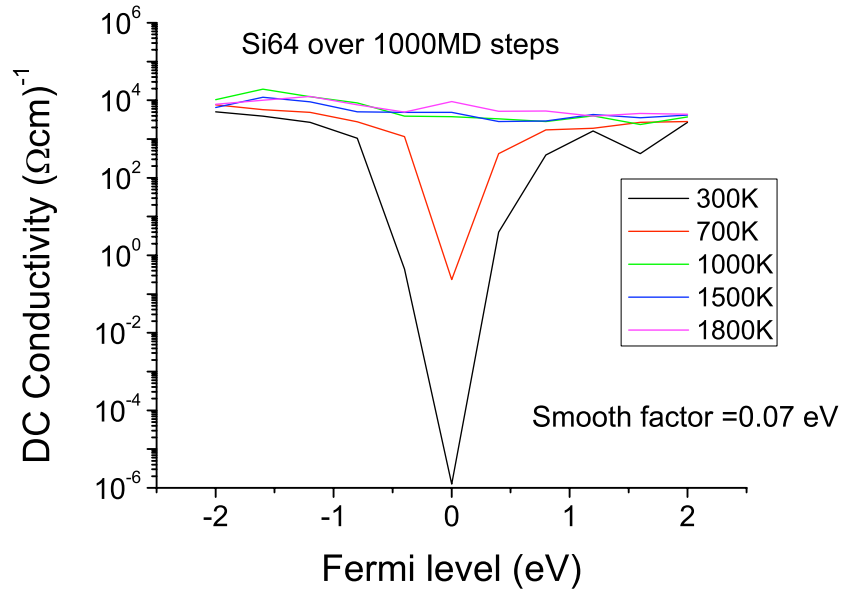

Figure A.1: DC conductivity of model a-Si64 at various temperatures and Fermi shifts.

It is necessary to point out one subtle factor that can affect the resulting values. There is a delta function in the DC Kubo-Greenwood formula. In numerical computation, due to the discrete nature, a delta function can only be approximated
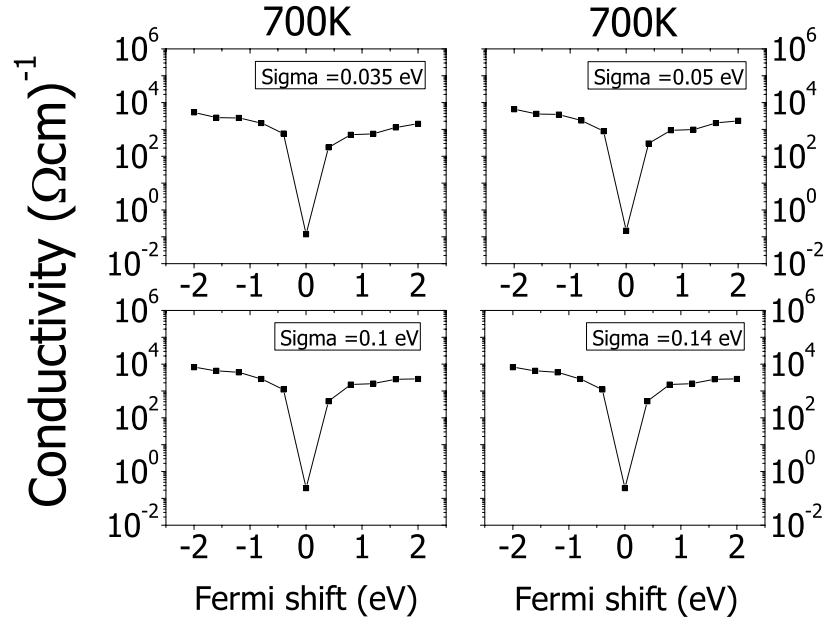
Figure A.2: DC conductivity at 700K for model a-Si64 at various smoothing factor Sigmas.

by a continuous function with a broadening (smoothing) factor σ. While a Gaussian function is easy to implement, the exact value of the broadening factor σ can affect the peak value of the delta function. To manifest σ dependence of the result, we plot Figure A.2. The 64-atom model a-Si64 is calculated at various σ (0.035eV, 0.05eV, 0.1eV and 0.14eV compared to the original 0.07eV) for 700K. We see that the results indeed vary according to σ. But the extent of the variation is small. The smallest energy interval between the states in our model is around 0.01 eV. For this reason our initial choice of σ as 0.07 eV is in principle a suitable value for the calculation.

A.1.2   Aluminum

Aside from a-Si, we applied our calculation on a metal, crystalline aluminum. We choose Al for our calculation for its simplicity in the psudopotential and band structure. We did the calculation on a 32 crystalline Al model, a 108 crystalline Al model and a 864 crystalline Al model. For the Al-108 model we also varied the temperature, considering 100K, 200K, 300K,400K,500K and 600K. The results are shown in Figure A.3.
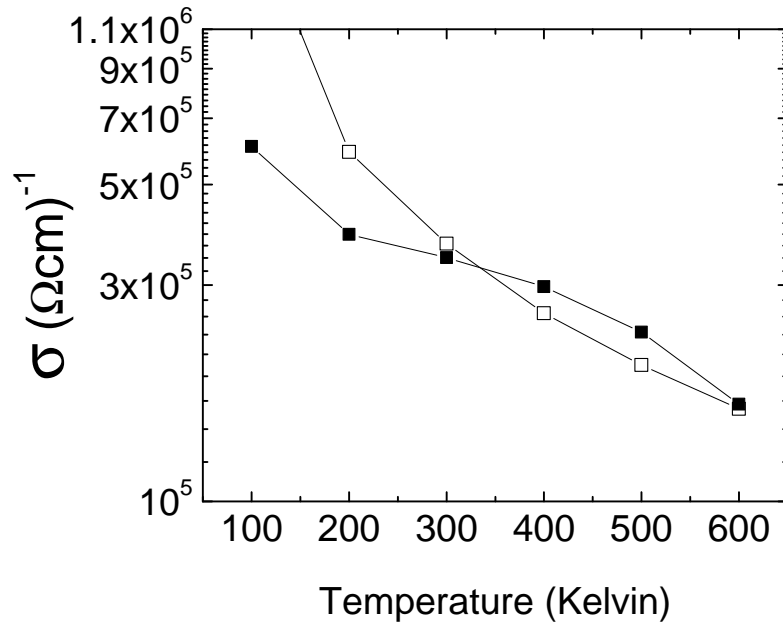

Figure A.3: DC conductivity at 100K, 200K, 300K, 400K, 500K and 600K by SIESTA DC from Aluminum model Al-108 (solid squares); reference [83] data at corresponding temperate is shown in open squares.

To measure the conductivity at each temperature, we equilibrate the model by molecular dynamics in SIESTA 2.0 for a long period (more than 5 ps) and the temperature stabilizes. The network always keeps crystalline structure and picks up lattice vibrations at each temperature. We then run the dc conductivity calculation for another 1 ps. The final result is averaged. The only numerical approximation we need to make again is the Gaussian broadening factor for the delta function. For each value point, we use 0.05 eV and 0.1 eV as the broadening factor and then average the result. For reason for using these specific values comes twofold: the smallest gap between energies appear to between 0.01 eV and 0.02 eV (about 1/5 of our chosen broadening value) for all our temperatures; a maximum value of conductivity is reached when the broadening factor lying between 0.05 eV and 0.1 eV.

We applied our dc conductivity calculation on Aluminum as a testing run, and we realized that in Aluminum the transport was scattering based. It was a little surprising for us that not only the results lies in reasonable range as compared to the reference values, the calculation was semi-quantitative for high temperatures. The Kubo-Greenwood formula appears to estimate the situation well. The lattice vibration (phonon) is not explicit in the formula, but the effect is taken into consideration when thermal averaging is applied. In principle, extensive MD process should sample a large number of phonon modes to make up a proper phonon spectrum. Temperature dependence is therefore properly reflected.

A.1.3 Summary

We modified code SIESTA 2.0 and implemented electrical conductivity calculation based on the Kubo-Greenwood formula. Calculation on a-Si and crystalline Aluminum have been applied and results shown. The comparisons to the experiments and former calculations were made and results suggested decent validity of our calculation and an unexpected success for our scheme of "adiabatic averaging". Further reliability of the code still needs to be tested and future applications will be needed.